

Model-agnostic assessment of dark energy after DESI DR1 BAO

Bikash R. Dinda ^{a,1} Roy Maartens ^{a,b,c}

^aDepartment of Physics & Astronomy, University of the Western Cape, Cape Town 7535, South Africa

^bInstitute of Cosmology & Gravitation, University of Portsmouth, Portsmouth PO1 3FX, United Kingdom

^cNational Institute for Theoretical & Computational Science, Cape Town 7535, South Africa

E-mail: bikashrdinda@gmail.com, roy.maartens@gmail.com

Abstract. Baryon acoustic oscillation measurements by the Dark Energy Spectroscopic Instrument (Data Release 1) have revealed exciting results that show evidence for dynamical dark energy at $\sim 3\sigma$ when combined with cosmic microwave background and type Ia supernova observations. These measurements are based on the w_0w_a CDM model of dark energy. The evidence is less in other dark energy models such as the w CDM model. In order to avoid imposing a dark energy model, we reconstruct the distance measures and the equation of the state of dark energy independent of any dark energy model and driven only by observational data. Our results show that the model-agnostic (in terms of late-time models) evidence for dynamical dark energy from DESI is not significant. Our analysis also provides model-independent constraints on cosmological parameters such as the Hubble constant and the matter-energy density parameter at present. Although we used CMB distance priors (not full CMB data) from a Λ CDM early-time model, our results remain largely similar for other cosmological models, provided that these models do not differ significantly from the standard model.

¹Corresponding author.

Contents

1	Introduction	2
2	Background equations	3
3	Observational data	4
3.1	DESI and other BAO data	4
3.2	CMB distance priors	5
3.3	Supernova data	6
4	Results	7
4.1	DESI DR1 and non-DESI BAO	7
4.2	CMB+DESI DR1 BAO and CMB+non-DESI BAO	10
4.3	DESI DR1 BAO+PantheonPlus	11
4.4	CMB+DESI DR1 BAO+PantheonPlus	13
4.5	CMB+Non-DESI BAO+PantheonPlus	14
4.6	Reconstructed constants and consistency check of Λ CDM	15
4.7	Hubble tension, M_B tension and their connection to w	17
5	Conclusions	17
A	Computation of $r_s(z_*)$ and r_d from CMB distance priors	19
B	Gaussian Process Regression	20
B.1	Single-task Gaussian Process regression up to second order derivative	20
B.1.1	Training the single-task GPR	20
B.1.2	Prediction from single-task GPR	21
B.2	Multi-task GP regression up to second-order derivative	22
B.2.1	Training the multi-task GPR	23
B.2.2	Prediction from multi-task GPR	24
B.3	Recovering single-task GPR from multi-task GPR	26
C	Notation used in the GPR analysis	27
D	Application of single-task GPR to PantheonPlus data and role of M_B	28
D.1	PantheonPlus+SHOES and CMB+PantheonPlus+SHOES	28
D.2	PantheonPlus, PantheonPlus+ M_B and CMB+PantheonPlus+ M_B	31
D.3	Extended list of reconstructed constants	31
E	Dependence on different CMB distance priors	32
F	Mean function dependence of GPR predictions	34

1 Introduction

Data Release 1 (DR1) from the new Dark Energy Spectroscopic Instrument (DESI) survey has produced exciting results from baryonic acoustic oscillation (BAO) measurements that seem to imply a degree of tension with the standard Λ CDM model of cosmology [1]. The initial DESI results have been extensively examined and used in follow-up work (e.g. [2–40]). The original DESI paper [1] favours a phantom behaviour of dark energy ($w < -1$) over a significant redshift range, with a preference for crossing to the non-phantom region at lower redshift. This conclusion arises when the dark energy equation of state in a late-time, spatially flat Friedmann-Lemaître-Robertson-Walker (FLRW) model is parametrised as [41, 42]

$$w(a) = w_0 + w_a(1 - a). \quad (1.1)$$

Here $a = (1 + z)^{-1}$ is the scale factor, where z is the cosmological redshift. This dark energy model generalises the standard Λ CDM model ($w_0 = -1, w_a = 0$), allowing for dynamical (evolving) dark energy at the cost of only 2 parameters. In addition, many possible dark energy models can be approximated by the w_0w_a CDM model.

However, there are various issues associated with using (1.1) to constrain dark energy evolution (see [7, 8, 43]). Although it facilitates the computation of a wide variety of dark energy evolutions, it is a phenomenological ansatz that is not based on a physical and self-consistent model of dark energy. In particular, there is no obstacle to the phantom regime $w < -1$, which is unphysical in general relativity (and in some modified gravity theories [39]), and the speed of sound of dark energy is arbitrary. By contrast, quintessence models of dark energy [2–7, 44–48] are physically self-consistent: there is no phantom regime and the quintessence speed of sound is always $c_s = c$ (speed of light in vacuum), which ensures that dark energy does not cluster and that causality is respected [49].

A disadvantage of assuming a physical quintessence model is that this rules out other non-standard models which can produce late-time acceleration. Examples are dark energy that is non-gravitationally coupled to dark matter [18–20, 50–54], and modified gravity models which produce late-time acceleration from modifications to general relativity [9–12, 55–57].

A model-agnostic approach is to avoid choosing a particular type of model so as to allow the data itself to constrain the evolution of w [24, 58, 59]. This approach can also incorporate non-standard models. In the case that modified gravity drives the late-time acceleration, w becomes an equation of state for the effective dark energy – i.e. the modified gravitational degree of freedom that mimics dark energy in the flat FLRW background. We limit our analysis to late-time accelerating models – i.e., models in which the (effective) dark energy does not affect the cosmic microwave background (CMB) or earlier processes in the young universe.

Machine learning provides various model-agnostic methods, including Gaussian Process (GP) regression [60–69], which enable data-driven reconstructions of the trends in the evolution of $w(z)$. In this paper, we apply GP regression to the DESI DR1 BAO data, combined with other data, in order to derive the behaviour of $w(z)$ that is consistent with the data sets and their errors.

The paper is organized as follows. In Section 2, we present the relevant spacetime and dynamical quantities in a flat late-time FLRW universe whose expansion is accelerating. We also express w in terms of BAO and supernova (SNIa) observables. Section 3 summarises the relevant observational data, including DESI DR1 and other BAO data, CMB distance data, and SNIa data. Appendix A gives details of CMB distance priors. Our results are given

in Section 4, using the multi-task GP methodology. Both the simple posterior (single-task) and the multi-task GP analysis are summarised in Appendix B, with Appendix C listing the notation used. Some applications of single-task GP to PantheonPlus data are discussed in Appendix D. We also address the effect on the results of (1) different CMB distance priors, in Appendix E, and (2) different GP mean functions and hyperparameters, in Appendix F. Our conclusions are presented in Section 5.

2 Background equations

Neglecting the contribution from radiation, in the flat FLRW metric, the Hubble parameter H for the late-time evolution is

$$\frac{H^2(z)}{H_0^2} = \Omega_{\text{m}0}(1+z)^3 + (1 - \Omega_{\text{m}0}) \exp \left[3 \int_0^z \frac{1+w(\tilde{z})}{1+\tilde{z}} d\tilde{z} \right], \quad (2.1)$$

where $\Omega_{\text{m}0}$ is the present value of the matter energy density parameter. The comoving radial distance and the Hubble radius are

$$D_M(z) = c \int_0^z \frac{d\tilde{z}}{H(\tilde{z})}, \quad (2.2)$$

$$D_H(z) = \frac{c}{H(z)}, \quad (2.3)$$

so that

$$D'_M(z) = D_H(z), \quad (2.4)$$

where a prime denotes d/dz .

From (2.1), we find w in terms of H and H' :

$$\begin{aligned} w(z) &= \frac{2(1+z)H(z)H'(z) - 3H^2(z)}{3[H^2(z) - \Omega_{\text{m}0}H_0^2(1+z)^3]} \\ &= -1 + \frac{2(1+z)H(z)H'(z) - 3\alpha(1+z)^3}{3[H^2(z) - \alpha(1+z)^3]}, \end{aligned} \quad (2.5)$$

where

$$\alpha = \Omega_{\text{m}0}H_0^2 = 10^4 \omega_{\text{m}0} \quad (\text{km/s/Mpc})^2. \quad (2.6)$$

Using (2.3) in (2.5) leads to

$$w(z) = -1 - \frac{2(1+z)D'_H(z) + 3\beta(1+z)^3 D_H^3(z)}{3[D_H(z) - \beta(1+z)^3 D_H^3(z)]}, \quad (2.7)$$

where

$$\beta = \frac{\alpha}{c^2} \approx 1.1126 \times 10^{-7} \omega_{\text{m}0} \quad \text{Mpc}^{-2}, \quad (2.8)$$

on using $H_0 \approx ch/(2998 \text{ Mpc})$. From (2.4) and (2.7), we find an alternative expression

$$w(z) = -1 - \frac{2(1+z)D''_M(z) + 3\beta(1+z)^3 D_M^3(z)}{3[D'_M(z) - \beta(1+z)^3 D_M^3(z)]}. \quad (2.9)$$

The anisotropic BAO measurements have data corresponding to the two observables

$$\tilde{D}_M(z) = \frac{D_M(z)}{r_d}, \quad \tilde{D}_H(z) = \frac{D_H(z)}{r_d}, \quad (2.10)$$

where r_d is the sound horizon at the baryon drag epoch. Using (2.4) and (2.10), we can rewrite (2.9) as

$$w(z) = -1 - \frac{2(1+z)\tilde{D}'_H(z) + 3\gamma(1+z)^3\tilde{D}_H^3(z)}{3[\tilde{D}_H(z) - \gamma(1+z)^3\tilde{D}_H^3(z)]}, \quad (2.11)$$

where

$$\gamma = \beta r_d^2 = \frac{\alpha r_d^2}{c^2} = \frac{\Omega_{\text{m}0} H_0^2 r_d^2}{c^2} \approx 1.1126 \times 10^{-7} \omega_{\text{m}0} \left(\frac{r_d}{\text{Mpc}} \right)^2. \quad (2.12)$$

Note that γ is a dimensionless constant, unlike α and β .

SNIa observations use the distance modulus μ_B as an observable, which is related to the luminosity distance d_L via

$$\mu_B(z) = m_B(z) - M_B = \frac{5}{\ln 10} \ln \left[\frac{d_L(z)}{\text{Mpc}} \right] + 25 \quad \text{where } d_L = (1+z)D_M. \quad (2.13)$$

Here m_B and M_B are the observed and absolute peak magnitudes of the supernova. Then

$$(1+z)D_M(z) = \exp \left\{ b [\mu_B(z) - 25] \right\} \text{ Mpc} \quad \text{where } b = \frac{\ln 10}{5}. \quad (2.14)$$

It is convenient to normalise D_M as

$$d_M(z) = e^{b(20+M_B)} D_M(z) = \frac{\exp \left\{ b [m_B(z) - 5] \right\}}{1+z} \text{ Mpc}. \quad (2.15)$$

Note that the constant $e^{b(20+M_B)}$ is defined in such a way that its magnitude is of $O(1)$. Using (2.15) we can rewrite (2.9) as

$$w(z) = -1 - \frac{2(1+z)d_M''(z) + 3\delta(1+z)^3 d_M^3(z)}{3[d_M'(z) - \delta(1+z)^3 d_M^3(z)]}, \quad (2.16)$$

where

$$\delta = \beta e^{-2b(20+M_B)} \approx 1.1126 \times 10^{-7} \left(\frac{\omega_{\text{m}0}}{\text{Mpc}^2} \right) e^{-2b(20+M_B)}. \quad (2.17)$$

3 Observational data

3.1 DESI and other BAO data

We mainly focus on five different DESI DR1 measurements of anisotropic BAO observables \tilde{D}_M and \tilde{D}_H at five different effective redshifts, z_{eff} . Two other measurements which correspond to the isotropic BAO observable are excluded, because of the difficulty to include these in a model-independent analysis. The mean, standard deviation, and correlation values of \tilde{D}_M and \tilde{D}_H at the five z_{eff} are shown in Table 1. In Table 1 and elsewhere ΔD indicates the standard deviation (1σ confidence level) of D and r is the correlation:

$$r[D_1, D_2] = \frac{\text{Cov}[D_1, D_2]}{\Delta D_1 \Delta D_2}. \quad (3.1)$$

We also consider other non-DESI anisotropic BAO data at another five different effective redshifts, as listed in Table 2.

	tracer (DESI DR1)	z_{eff}	$\tilde{D}_M \pm \Delta\tilde{D}_M$	$\tilde{D}_H \pm \Delta\tilde{D}_H$	$r[\tilde{D}_M, \tilde{D}_H]$	Refs.
1	LRG	0.510	13.62 ± 0.25	20.98 ± 0.61	-0.445	[70]
2	LRG	0.706	16.85 ± 0.32	20.08 ± 0.60	-0.420	[70]
3	LRG+ELG	0.930	21.71 ± 0.28	17.88 ± 0.35	-0.389	[1]
4	ELG	1.317	27.79 ± 0.69	13.82 ± 0.42	-0.444	[71]
5	Ly- α	2.330	39.71 ± 0.94	8.52 ± 0.17	-0.477	[1]

Table 1. Measurements of anisotropic BAO observables \tilde{D}_M and \tilde{D}_H and correlations between them at five different effective redshifts from DESI DR1 BAO data [1].

	tracer (non-DESI BAO)	z_{eff}	$\tilde{D}_M \pm \Delta\tilde{D}_M$	$\tilde{D}_H \pm \Delta\tilde{D}_H$	$r[\tilde{D}_M, \tilde{D}_H]$	Refs.
1	LRG (BOSS DR12)	0.38	10.234 ± 0.151	24.981 ± 0.582	-0.228	[72]
2	LRG (BOSS DR12)	0.51	13.366 ± 0.179	22.317 ± 0.482	-0.233	[72]
3	LRG (eBOSS DR16)	0.698	17.858 ± 0.302	19.326 ± 0.469	-0.239	[73]
4	QSO (eBOSS DR16)	1.48	30.688 ± 0.789	13.261 ± 0.469	0.039	[74]
5	Ly- α QSO (eBOSS DR16)	2.334	37.5 ± 1.2	8.99 ± 0.19	-0.45	[75]

Table 2. Measurements of anisotropic BAO observables \tilde{D}_M and \tilde{D}_H and correlations between them at five different effective redshifts from non-DESI BAO data [73].

3.2 CMB distance priors

The late-time cosmological data analysis can be done with three CMB parameters instead of the full CMB likelihood [25, 76–79]:

$$R = \frac{1}{c} (\Omega_{\text{m}0} H_0^2)^{1/2} D_M(z_*), \quad (3.2)$$

$$l_A = \frac{\pi D_M(z_*)}{r_s(z_*)}, \quad (3.3)$$

$$\omega_{\text{b}0} = \Omega_{\text{b}0} h^2, \quad (3.4)$$

where z_* is the photon decoupling redshift, R is the CMB shift parameter, l_A is the acoustic length scale at z_* , $\Omega_{\text{b}0}$ is the present value of the baryonic density parameter, and r_s is the sound horizon. Because $D_M(z_*)$ appears in both R and l_A , we can not individually use these two parameters in a model-independent data analysis. For this purpose, the ratio \tilde{R} of these two parameters is used. Then the mean and standard deviation of the two CMB parameters, from Planck 2018 results for TT, TE, EE+lowE+lensing (considering the standard model, i.e. the base Λ CDM model) are [80]

$$\tilde{R} = \frac{R}{l_A} = \frac{\omega_{\text{m}0}^{1/2}}{3000\pi} \frac{r_s(z_*)}{\text{Mpc}} = 0.005797 \pm 0.000013, \quad (3.5)$$

$$\omega_{\text{b}0} = \Omega_{\text{b}0} h^2 = 0.02237 \pm 0.00015, \quad (3.6)$$

$$r[\tilde{R}, \omega_{\text{b}0}] = -0.61. \quad (3.7)$$

In order to find the above values, we use the Planck 2018 data archive for the base Λ CDM model, in the chain `base_plikHM_TTTEEE_lowl_lowE_lensing`.

In standard early-time physics approximations, the sound horizon at photon decoupling $r_s(z_*)$ becomes a function of only ω_{m0} and ω_{b0} . For details, see Appendix A. In this case, \tilde{R} is also a function of only ω_{m0} and ω_{b0} . Using this assumption and solving (3.5)–(3.7), we find

$$\omega_{m0} = 0.1430 \pm 0.0011 , \quad (3.8)$$

$$r[\omega_{b0}, \omega_{m0}] = -0.42 . \quad (3.9)$$

In addition, the sound horizon $r_d = r_s(z_d)$ at the baryon drag epoch z_d is also a function of only ω_{m0} and ω_{b0} . Using (3.6), (3.8), and (3.9), we have

$$r_d = 146.995 \pm 0.264 \text{ Mpc}, \quad (3.10)$$

and the normalised covariance between ω_{m0} and r_d is

$$r[\omega_{m0}, r_d] = -0.90 . \quad (3.11)$$

To cross-check these values, we use a fitting formula from [1] [their eq. (2.5)]:

$$\frac{r_d}{\text{Mpc}} = 147.05 \left(\frac{\omega_{m0}}{0.1432} \right)^{-0.23} \left(\frac{\omega_{b0}}{0.02236} \right)^{-0.13} . \quad (3.12)$$

Here we used the standard value 3.04 for the effective number of relativistic species. From (3.6), (3.8), and (3.9) we obtain

$$r_d = 147.089 \pm 0.237 \text{ Mpc}, \quad (3.13)$$

which is consistent with (3.10). We use (3.10) for our analysis.

From the above constraints we find constraints on α , β and γ :

$$\alpha \approx 1430 \pm 11 \text{ (km/s/Mpc)}^2 , \quad (3.14)$$

$$\beta \approx (159.1 \pm 1.2) \times 10^{-10} \text{ Mpc}^{-2} , \quad (3.15)$$

$$\gamma \approx (343.8 \pm 1.6) \times 10^{-6} . \quad (3.16)$$

These results are our CMB data.

Throughout our analysis, we consider priors on these parameters as an alternative to the full CMB likelihood. The prior values of α , β , and γ , obtained using the base Λ CDM model from compressed CMB data, are a good approximation to, and a simplified version of, the full CMB data, provided that the true model of the Universe does not deviate significantly from Λ CDM [77, 78]. We also note that the values of these parameters would be slightly different for other cosmological models. Still, the main result, i.e. the reconstruction of the equation of state of dark energy, does not differ significantly when we consider other models beyond Λ CDM. We emphasize that the use of the base Λ CDM model does not significantly bias our result toward a Λ CDM value – as shown explicitly in Appendix E.

3.3 Supernova data

We consider the Pantheon+ sample – which we denote PantheonPlus – for SNIa data on the apparent magnitude m_B . This consists of 1701 light curves for 1550 spectroscopically

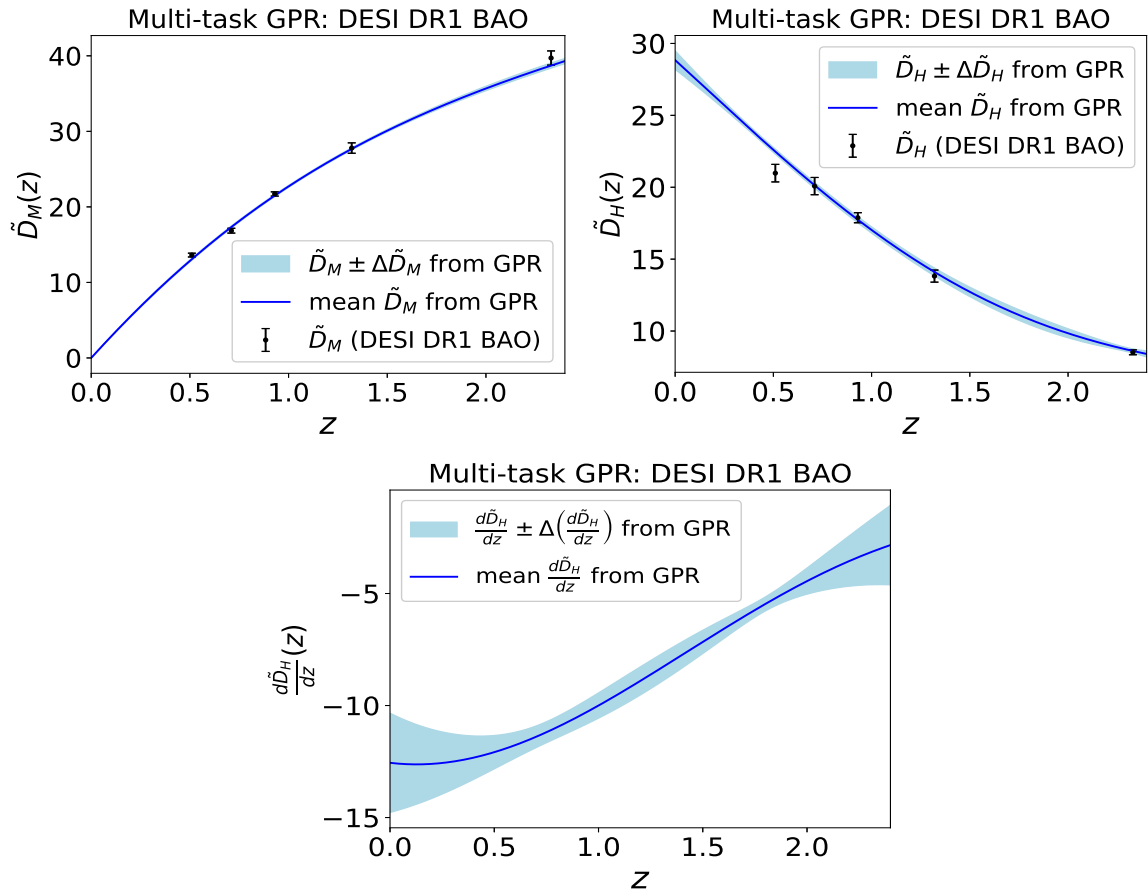


Figure 1. Reconstruction of \tilde{D}_M (top left), $\tilde{D}'_M = \tilde{D}_H$ (top right), and $\tilde{D}''_M = \tilde{D}'_H$ (bottom) from DESI DR1 BAO data (Table 1), using multi-task Gaussian Process regression. Blue regions are the reconstructed 1σ confidence intervals. Blue solid lines are the best-fit values. In the top panels, black error bars correspond to the DESI DR1 BAO data.

confirmed SNIa in the redshift range $0.00122 \leq z \leq 2.26137$ [81]. We exclude 111 light curves at low redshifts, $z < 0.01$, in order to avoid strong peculiar velocity dependence [82]. In our analysis, we define the sub-sample

$$\text{PantheonPlus: } 1590 \text{ light curves in } 0.01016 \leq z \leq 2.26137. \quad (3.17)$$

We consider the full statistical and systematic covariance for this data, which can be found at <https://github.com/PantheonPlusSHOES/DataRelease>.

4 Results

In this section, we apply the GP regression (GPR) methodology, which is described in Appendix B, to the datasets, in order to reconstruct the distances and then the dark energy (or effective dark energy) equation of state w .

4.1 DESI DR1 and non-DESI BAO

We start with the DESI DR1 BAO data of \tilde{D}_M and $\tilde{D}_H (= \tilde{D}'_M)$. Because \tilde{D}_M and \tilde{D}_H are correlated and the correlations are large, we cannot simply use the simple single-task GPR,

discussed in Section B.1, individually to \tilde{D}_M and \tilde{D}_H . Instead, we need the multi-task GPR, which deals with the covariance between a variable and its derivative (see Section B.2). In detail:

- $X_1 = X_2 = \{z_{\text{eff}}\}$ is the vector of all effective redshift points.
- $Y_1 = \{\tilde{D}_M\}$ is the vector of all mean values of \tilde{D}_M .
- $Y_2' = \{\tilde{D}_H\} = Y_1'$ (since $X_2 = X_1$) is the vector of all mean values of $\tilde{D}'_M = \tilde{D}_H$.
- $C_{11} = \{\text{Cov}[\tilde{D}_M, \tilde{D}_M]\}$ is the matrix of all self-covariances of \tilde{D}_M .
- $C_{12}^{(0,1)} = \{\text{Cov}[\tilde{D}_M, \tilde{D}_H]\}$ is matrix of all cross covariances between \tilde{D}_M and \tilde{D}_H .
- $C_{21}^{(1,0)} = \{\text{Cov}[\tilde{D}_H, \tilde{D}_M]\} = (\{\text{Cov}[\tilde{D}_M, \tilde{D}_H]\})^T = (C_{12}^{(0,1)})^T$ is the matrix of all cross covariances between \tilde{D}_H and \tilde{D}_M .
- $C_{22}^{(1,1)} = \{\text{Cov}[\tilde{D}_H, \tilde{D}_H]\}$ is the matrix of all self-covariances of \tilde{D}_H .

We consider the most popular kernel covariance function, the squared-exponential, in which the kernel covariance between x_1 and x_2 is

$$k(x_1, x_2) = \sigma_f^2 \exp \left[- \frac{(x_1 - x_2)^2}{l^2} \right], \quad (4.1)$$

where σ_f and l are the two kernel hyperparameters. Note that one has to choose a kernel that is differentiable at least up to the order at which we want the prediction from GPR. The squared exponential kernel is infinitely differentiable. For this reason, it can be used in any GPR task for the prediction of any order of the function.

We also need a mean function to perform a GPR task. We choose the zero mean function to avoid any cosmological model-dependent bias

$$\mu(x) = 0. \quad (4.2)$$

Similarly to the kernel, the mean function needs to be differentiable up to the order we want the prediction. The zero mean function is infinitely differentiable and at any order, it is always the zero mean function.

Although the zero mean function is a popular choice to avoid any cosmological model-dependent bias, if the quality of data is not good enough, then the GP reconstruction will have a bias towards the zero values. The same applies to any other mean function assumed [83]. If the quality of data is good, then the reconstructed results of GP will not be significantly biased towards a chosen mean function. Fortunately, the data combinations we consider here are good enough to put reasonable constraints on the expansion history of the Universe and the zero mean function is a safe choice in our analysis. We show this in detail in Appendix F.

We use the above information in (B.27)–(B.46) in order to compute the negative log marginal likelihood. This is a function of the kernel hyperparameters, including mean function parameters and other parameters (if present). We then minimise the negative of this log marginal likelihood to find the best-fit values of all the parameters.

These best-fit parameter values are used in the prediction of the functions F_* (here \tilde{D}_M), F'_* (here $\tilde{D}'_M = \tilde{D}_H$), and F''_* (here $\tilde{D}''_M = \tilde{D}'_H$) at target redshift points. We want predictions

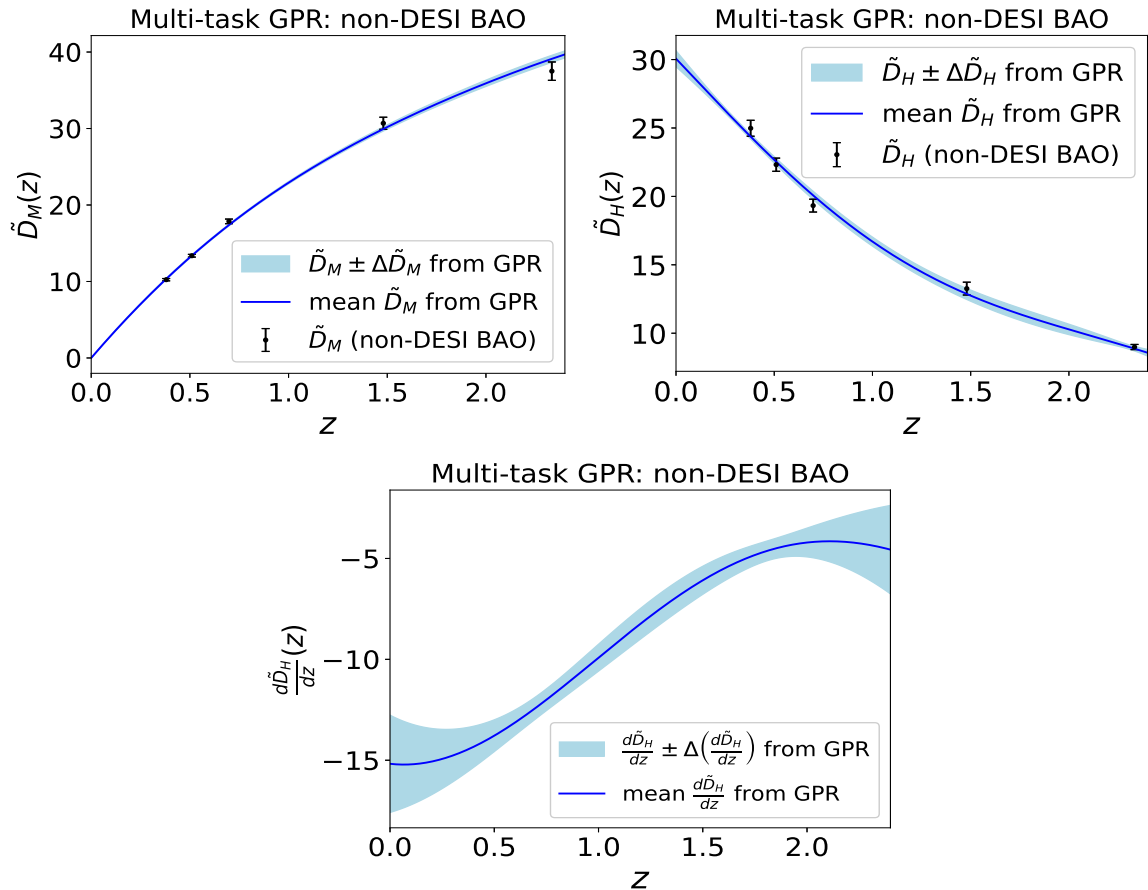


Figure 2. As in Fig. 1, for non-DESI BAO data (Table 2).

for smooth functions of redshift z . To do so, we need to consider a large number of target points, and we use

$$X_* = \text{a vector of 1000 equispaced redshift points in } 0 \leq z \leq 2.4. \quad (4.3)$$

Finally, we obtain the mean values of \tilde{D}_M (corresponding to \bar{F}_*) using (B.55) and the corresponding 1σ confidence region from the prediction of the square root of self-covariances (variances at each target point) using (B.59). We plot these values in the top left panel of Fig. 1. The mean function is represented by the solid blue line and the 1σ region is represented by the blue shading. To compare the predicted outcome of the GPR with the actual DESI DR1 BAO data, we also plot the \tilde{D}_M data with black error bars.

We see that the predictions are quite consistent with the data. Similarly, we get the mean and standard deviation values of $\tilde{D}'_M = \tilde{D}_H$ (corresponding to \bar{F}'_*) using (B.56) and (B.60), shown in the top right panel of Fig. 1. We compare this prediction with the DESI DR1 BAO data by plotting the \tilde{D}_H data with black error bars. Here the predictions are also consistent with the data.

Predictions for the mean and standard deviation of $\tilde{D}''_M = \tilde{D}'_H$ (corresponding to \bar{F}''_*), using (B.57) and (B.61), are displayed in the bottom panel of Fig. 1. Note that for this second-order derivative prediction, there is no data for comparison with the predicted outcomes.

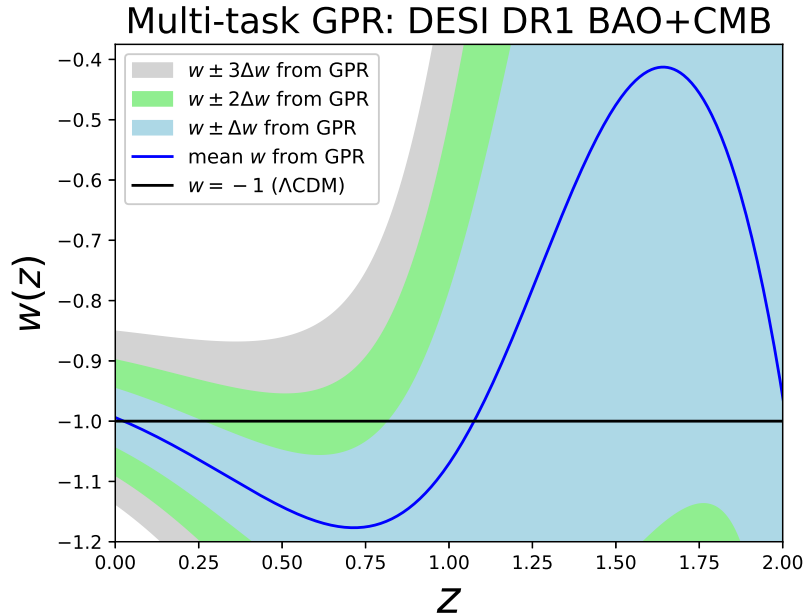


Figure 3. Reconstructed redshift evolution of equation of state of (effective) dark energy (w), obtained via (2.11) from the reconstructed \tilde{D}'_M and \tilde{D}''_M (from DESI DR1 BAO with multi-task GPR), with the constraints on γ obtained from (3.16) (Planck 2018 CMB). Blue, green, and grey shadings are the 1σ , 2σ , and 3σ confidence intervals of w . The blue line is the best-fit value of w and the black line is $w = -1$ (Λ CDM).

For the non-DESI BAO, we follow the same procedure to compute the predicted mean functions of \tilde{D}_M , $\tilde{D}'_M = \tilde{D}_H$, and $\tilde{D}''_M = \tilde{D}''_H$ and the corresponding 1σ regions. These are shown in Fig. 2 with the same color codes. The non-DESI BAO data are shown as black points with error bars. We find again that the predicted values are consistent with the data.

4.2 CMB+DESI DR1 BAO and CMB+non-DESI BAO

Next, from the reconstructed values of \tilde{D}'_M , and \tilde{D}''_M , we compute the redshift evolution of w using (2.11). Note that in order to compute w , we also need the value of γ given in (3.16), which we find from Planck 2018 CMB results (considering standard early time physics) for TT, TE, EE+lowE+lensing. Thus computation of w requires a combination of DESI DR1 BAO data and CMB data, denoted as CMB+DESI DR1 BAO. Also note that when we compute the errors in w using the propagation of uncertainty, we need values of the cross covariances between \tilde{D}'_M and \tilde{D}''_M along with their self-covariances (variances). We compute these cross covariances using (B.64). The reconstructed mean function of w (blue line) and the 1σ (blue), 2σ (green + blue) and 3σ (grey + green + blue) confidence regions are displayed in Fig. 3.

It is evident that for the redshift range $0 \lesssim z \lesssim 1$, the best-fit equation of state is phantom and the Λ CDM model is $\sim 1 - 1.5\sigma$ away. Around $z = 1.05$, there is a phantom crossing and after that w is non-phantom. However, this phantom crossing is not that significant, because the Λ CDM model is within the 1σ limit at $z \gtrsim 0.8$.

For the CMB+non-DESI BAO data, we follow the same procedure to compute w and the associated errors. The results are shown in Fig. 4 with the same color codes as in Fig. 3.

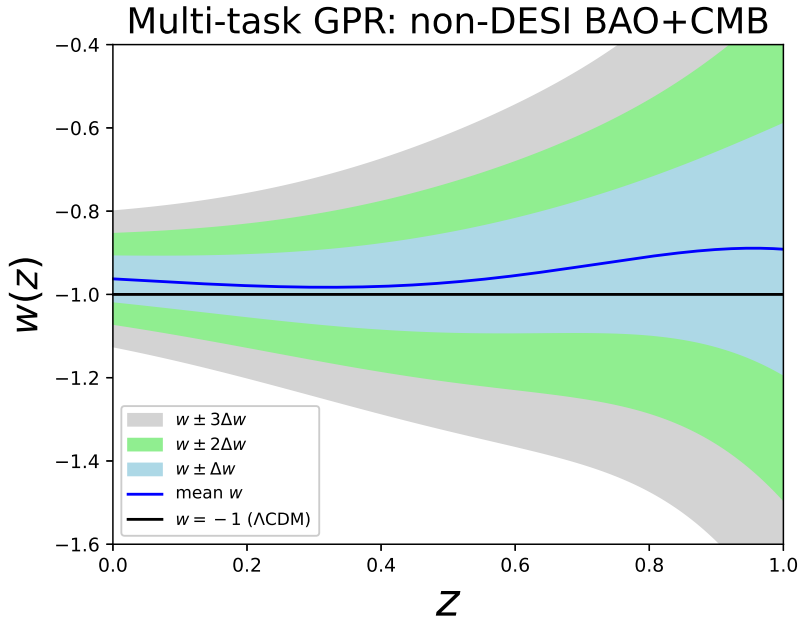


Figure 4. As in Fig. 3, for CMB+non-DESI BAO (multi-task GPR).

In the non-DESI case, the Λ CDM model is well within the 1σ region for the entire redshift range.¹

4.3 DESI DR1 BAO+PantheonPlus

Next, we combine DESI DR1 data with PantheonPlus data. We do not consider any M_B priors, since the combination of these datasets can in principle constrain the M_B parameter using the CMB constraint on r_d . This can be seen through the connection between variables d_M and \tilde{D}_M : from (2.10) and (2.15), we find

$$d_M(z) = \zeta \tilde{D}_M(z), \quad (4.4)$$

$$\zeta = r_d e^{b(20+M_B)} \quad (4.5)$$

Similarly, using (2.4) and (4.4), we get

$$d'_M(z) = d'_H(z) = \zeta \tilde{D}'_M(z) = \zeta \tilde{D}'_H(z), \quad (4.6)$$

$$d''_M(z) = d''_H(z) = \zeta \tilde{D}''_M(z) = \zeta \tilde{D}''_H(z). \quad (4.7)$$

These equations suggest that a combination of SNIa and BAO observations constrains the parameter ζ . We use d_M from BAO as a function of ζ via (4.4). We also use the PantheonPlus d_M . We then apply multi-task GPR, where the first derivative information is provided by d'_M

¹Note that our results are based on the BAO data, which may change if either the primordial or late-time model or both are far from the fiducial model used to obtain the BAO data [84–88].

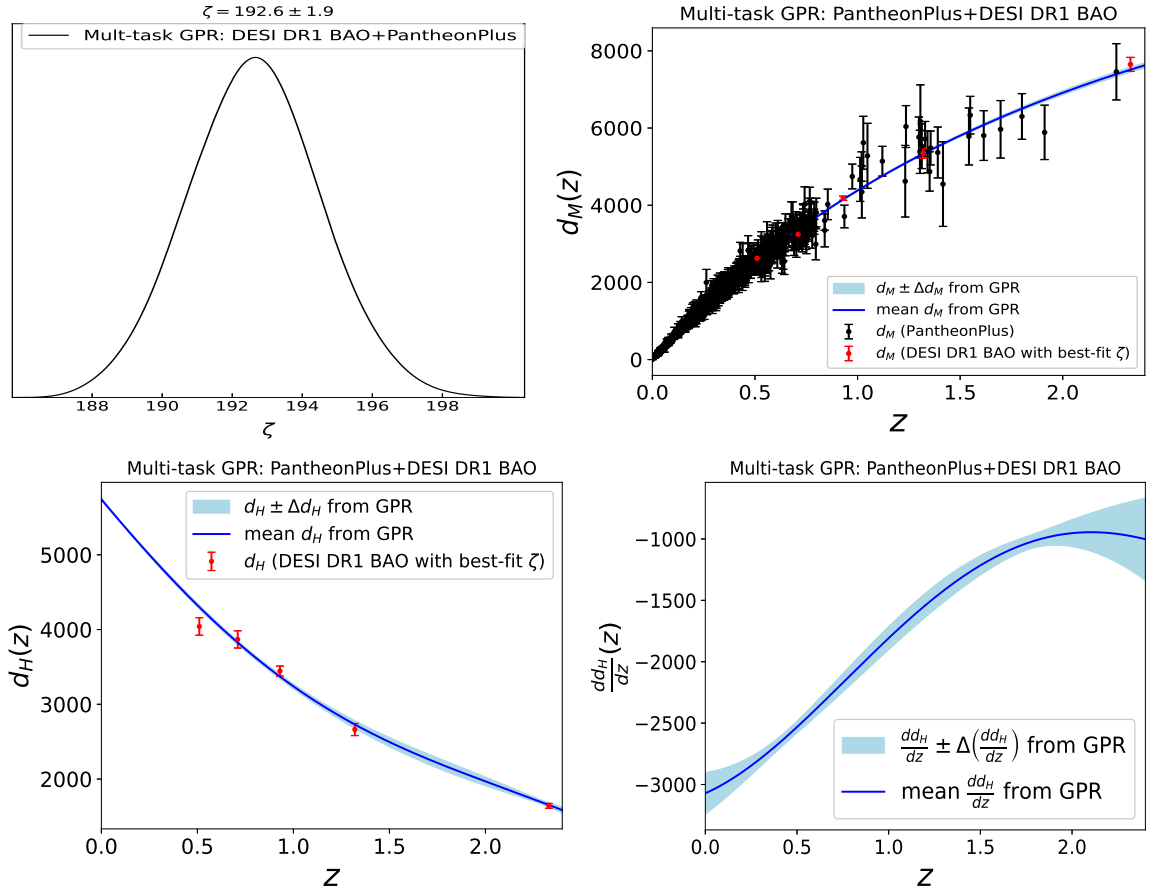


Figure 5. Multi-task GPR analysis of the combination DESI DR1 BAO+PantheonPlus. Marginalised probability distribution of ζ parameter (top left). Black error bars (top right) show $d_M \pm \Delta d_M$ from observed m_B of PantheonPlus data, using (2.15) (as in Fig. 10). Red error bars show $d_M \pm \Delta d_M$ for DESI DR1 BAO from \tilde{D}_M (top right) or $d_H \pm \Delta d_H$ from \tilde{D}_H (bottom left), using the constraint on ζ . Blue solid lines and shadings in the top right, bottom left, and bottom right panels correspond to reconstructed d_M , $d'_M = d_H$, $d''_M = d'_H$, and associated 1σ confidence regions.

($= d_H$) from DESI DR1 BAO as a function of ζ using (4.6). This corresponds to

$$X_1 = \begin{bmatrix} \{z_{\text{eff}}\} \text{ (DESI DR1 BAO)} \\ \{z\} \text{ (PantheonPlus)} \end{bmatrix}, \quad (4.8)$$

$$X_2 = \{z_{\text{eff}}\} \text{ (DESI DR1 BAO)}, \quad (4.9)$$

$$Y_1 = \begin{bmatrix} \{d_M(\zeta)\} \text{ (DESI DR1 BAO)} \\ \{d_M\} \text{ (PantheonPlus)} \end{bmatrix}, \quad (4.10)$$

$$Y'_2 = \{d'_M(\zeta) = d_H(\zeta)\} \text{ (DESI DR1 BAO)}. \quad (4.11)$$

Then we perform a multi-task GPR analysis. Minimisation of the negative log marginal likelihood provides constraints on kernel hyperparameters as well as on ζ :

$$\text{DESI DR1 BAO+PantheonPlus: } \zeta = 192.6 \pm 1.9 \text{ Mpc}. \quad (4.12)$$

The marginalised probability of ζ obtained from the minimisation is shown in the top left panel of Fig. 5.

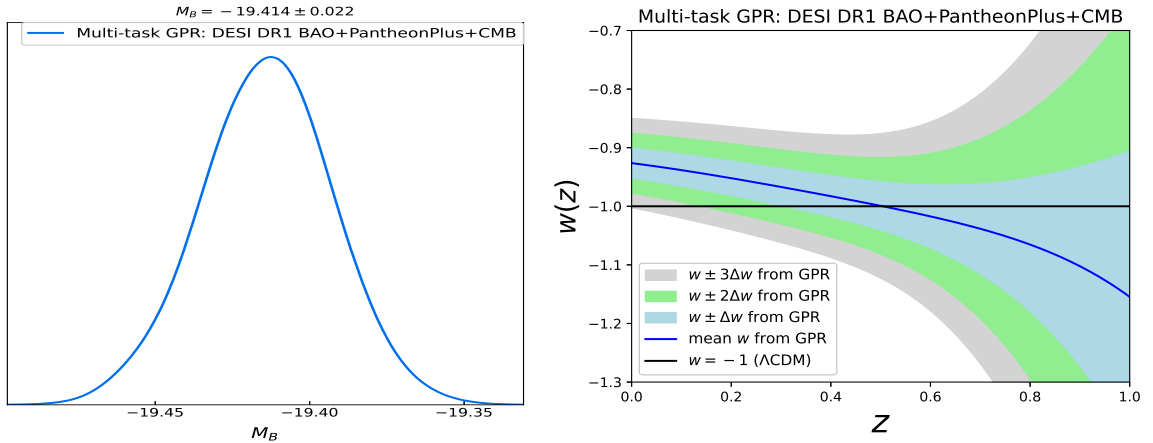


Figure 6. For the combination CMB+DESI DR1 BAO+PantheonPlus (multi-task GPR), the left panel shows the marginalised probability of the M_B parameter, obtained from constraints on ζ and from the r_d Gaussian prior in (3.10). The reconstructed w and associated confidence regions are displayed in the right panel, using (2.16), (2.17) and (3.15) with the obtained M_B constraints.

In the top right panel of Fig. 5, we plot the reconstructed d_M and associated 1σ confidence (solid blue line and shading). The black error bars (top right) show $d_M \pm \Delta d_M$ obtained directly from PantheonPlus data of m_B using (2.15). The red error bars also correspond to $d_M \pm \Delta d_M$ but obtained from DESI DR1 BAO data of \tilde{D}_M , using the constraint on ζ in (4.12). We see that the obtained reconstructed function of d_M from multi-task GPR is consistent with the d_M obtained from both PantheonPlus and DESI DR1 BAO data.

The predicted $d'_M = d'_H$ and associated 1σ confidence interval are shown in the bottom left panel of Fig. 5 in blue. In the same panel, the red error bars correspond to $d'_H \pm \Delta d'_H$ obtained from DESI DR1 BAO data of \tilde{D}_M and constraints on ζ using (4.12). It is evident that the predicted d'_H is consistent with the d'_H obtained from DESI DR1 BAO (with ζ value).

Similarly, the predicted second derivative $d''_M = d''_H$ and the associated 1σ confidence region are shown in the bottom right panel of Fig. 5. In this case, there is no data to compare the predicted outcome from multi-task GPR.

4.4 CMB+DESI DR1 BAO+PantheonPlus

In the left panel of Fig. 6, we plot the marginalised probability of the M_B parameter. This is obtained using the ζ constraint and the r_d Gaussian prior mentioned in (4.12) and (3.10) respectively. Because we include r_d prior from CMB to break the degeneracy between r_d and M_B , this corresponds to the inclusion of CMB data and the constraint on M_B from CMB + DESI DR1 BAO + PantheonPlus is

$$\text{CMB+DESI DR1 BAO+PantheonPlus: } M_B = -19.414 \pm 0.022 \text{ mag.} \quad (4.13)$$

Note that this value of M_B is smaller than the SHOES value.

From the reconstructed d'_M , d''_M , constraint on M_B from (4.13), and constraint on β from (3.15), we compute w and the associated errors using (2.16) and (2.17). These are plotted in the right panel of Fig. 6. The solid blue line, the blue region, the green region (including the blue region), and the gray region (including blue and green regions) correspond to the mean function of w , associated 1σ , 2σ , 3σ confidence regions respectively. We see that at lower

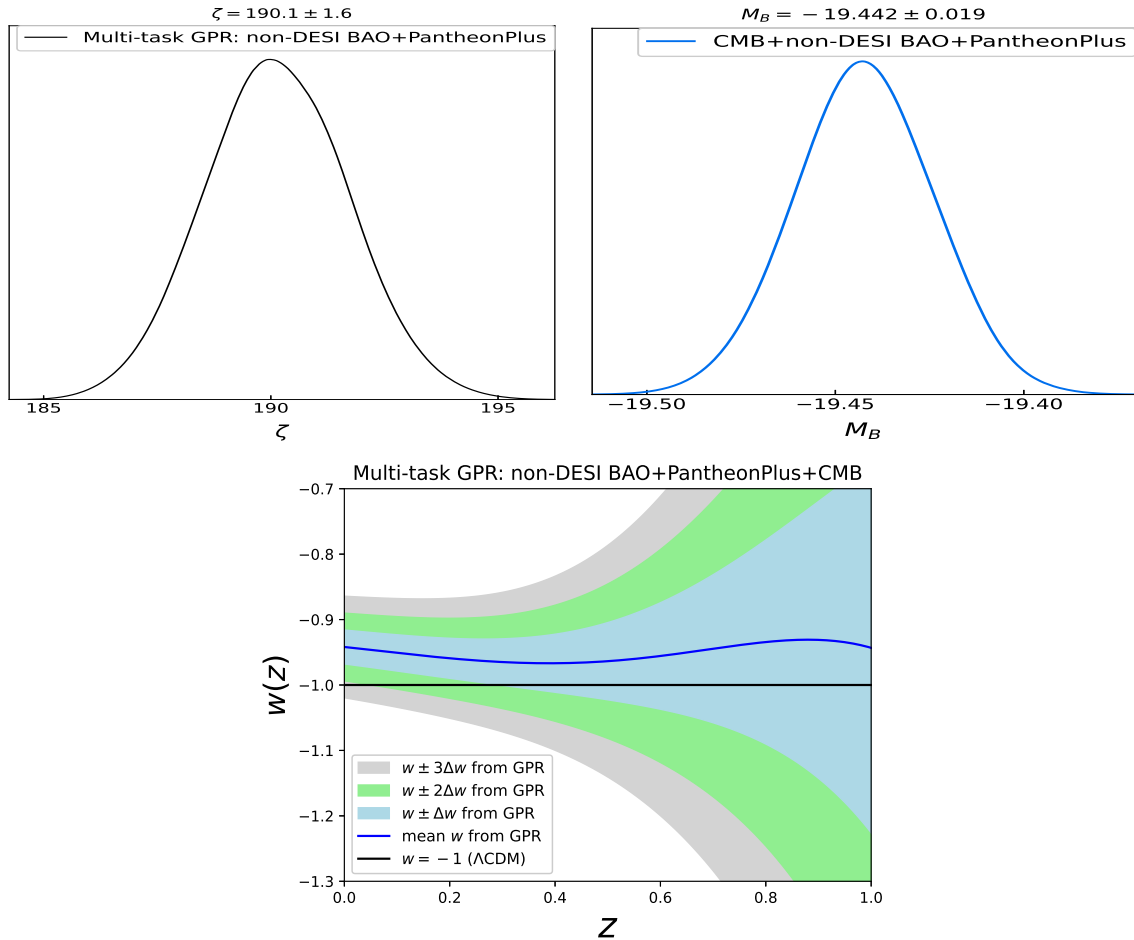


Figure 7. Non-DESI BAO+PantheonPlus and CMB+non-DESI BAO+PantheonPlus combinations, using multi-task GPR. Top panels: marginalised probabilities of ζ , without CMB (left) and of M_B , with CMB (right). Reconstructed w and associated confidence regions are shown in the bottom panel for CMB+non-DESI BAO+PantheonPlus (multi-task GPR) using the same methodology as for Figs. 5 and 6.

redshifts $0 < z < 0.5$ non-phantom regions are preferable for the CMB + DESI DR1 BAO + PantheonPlus combination of data. In this redshift region, the Λ CDM model is around more than 2σ to less than 1σ away (gradually decreasing with increasing redshift) from the reconstructed mean of w and in other redshift regions, it is well within the 1σ confidence regions.

4.5 CMB+Non-DESI BAO+PantheonPlus

For the non-DESI BAO data, we start with the multi-task GPR combination with PantheonPlus, without using CMB information. We find a constraint on ζ ,

$$\text{non-DESI BAO+PantheonPlus: } \zeta = 190.1 \pm 1.6 \text{ Mpc.} \quad (4.14)$$

Introducing CMB data via r_d constraints, we obtain constraints on the M_B parameter for CMB+non-DESI BAO+PantheonPlus:

$$\text{CMB+non-DESI BAO+PantheonPlus: } M_B = -19.442 \pm 0.019 \text{ mag.} \quad (4.15)$$

Data combination	$H_0 r_d$ [100 km/s]	H_0 [km/s/Mpc]	Ω_{m0}	M_B [mag]
DESI	104.02 ± 2.34	-	-	-
non-DESI	99.78 ± 1.94	-	-	-
DESI+PP	100.65 ± 1.03	-	-	-
non-DESI+PP	99.30 ± 0.87	-	-	-
CMB+DESI	104.02 ± 2.34	70.74 ± 1.60	0.286 ± 0.013	-
CMB+non-DESI	99.78 ± 1.94	67.86 ± 1.33	0.310 ± 0.013	-
CMB+DESI+PP	100.65 ± 1.03	68.45 ± 0.71	0.305 ± 0.007	-19.414 ± 0.022
CMB+non-DESI+PP	99.30 ± 0.87	67.53 ± 0.61	0.313 ± 0.006	-19.442 ± 0.019

Table 3. Reconstructed values of $H_0 r_d$, H_0 , Ω_{m0} and M_B . PP denotes PantheonPlus data (3.17).

Note that this value is slightly smaller than the one obtained from CMB + DESI DR1 BAO + PantheonPlus in (4.13). The corresponding marginalised probabilities of ζ and M_B are shown in the top left and top right panels of Fig. 7.

Following the same methodology as in the previous case, we reconstruct w and the associated confidence regions. These are displayed in the bottom panel of Fig. 7. We find that in the redshift range $0 < z \lesssim 0.35$, the reconstructed w is preferably in the non-phantom region at more than 1σ confidence. In the same redshift range, the Λ CDM model is around 2σ to 1σ away and in other regions, it is well within the 1σ region.

4.6 Reconstructed constants and consistency check of Λ CDM

Once we have all the corresponding reconstructed functions and consequently their values at present ($z = 0$), we obtain constraints on the constants used in the cosmological analysis. We compute these constants using combinations of data sets as follows:

$$\text{BAO: } H_0 r_d = \frac{c}{\tilde{D}_H(z=0)}, \quad (4.16)$$

$$\text{BAO+SNIa: } H_0 r_d = \frac{c\zeta}{d_H(z=0)}, \quad (4.17)$$

$$\begin{aligned} \text{CMB+BAO: } H_0 r_d &= \frac{c}{\tilde{D}_H(z=0)} \text{ (same as for only BAO),} \\ H_0 &= \frac{c}{r_d \tilde{D}_H(z=0)}, \quad \Omega_{m0} = \frac{\omega_{m0}}{h^2}, \end{aligned} \quad (4.18)$$

$$\begin{aligned} \text{CMB+BAO+SNIa: } H_0 r_d &= \frac{c\zeta}{d_H(z=0)} \text{ (same as for BAO+SNIa),} \\ H_0 &= \frac{c\zeta}{r_d d_H(z=0)}, \quad \Omega_{m0} = \frac{\omega_{m0}}{h^2}, \quad M_B = \frac{1}{b} \ln \left(\frac{\zeta}{r_d} \right) - 20. \end{aligned} \quad (4.19)$$

The mean and standard deviation values are listed in Table 3.

Once we know H_0 and Ω_{m0} separately, we can check the consistency of the Λ CDM model with different combinations of data in another way through the parameter

$$f_{\text{DE}}(z) = \exp \left[3 \int_0^z \frac{1+w(\tilde{z})}{1+\tilde{z}} d\tilde{z} \right]. \quad (4.20)$$

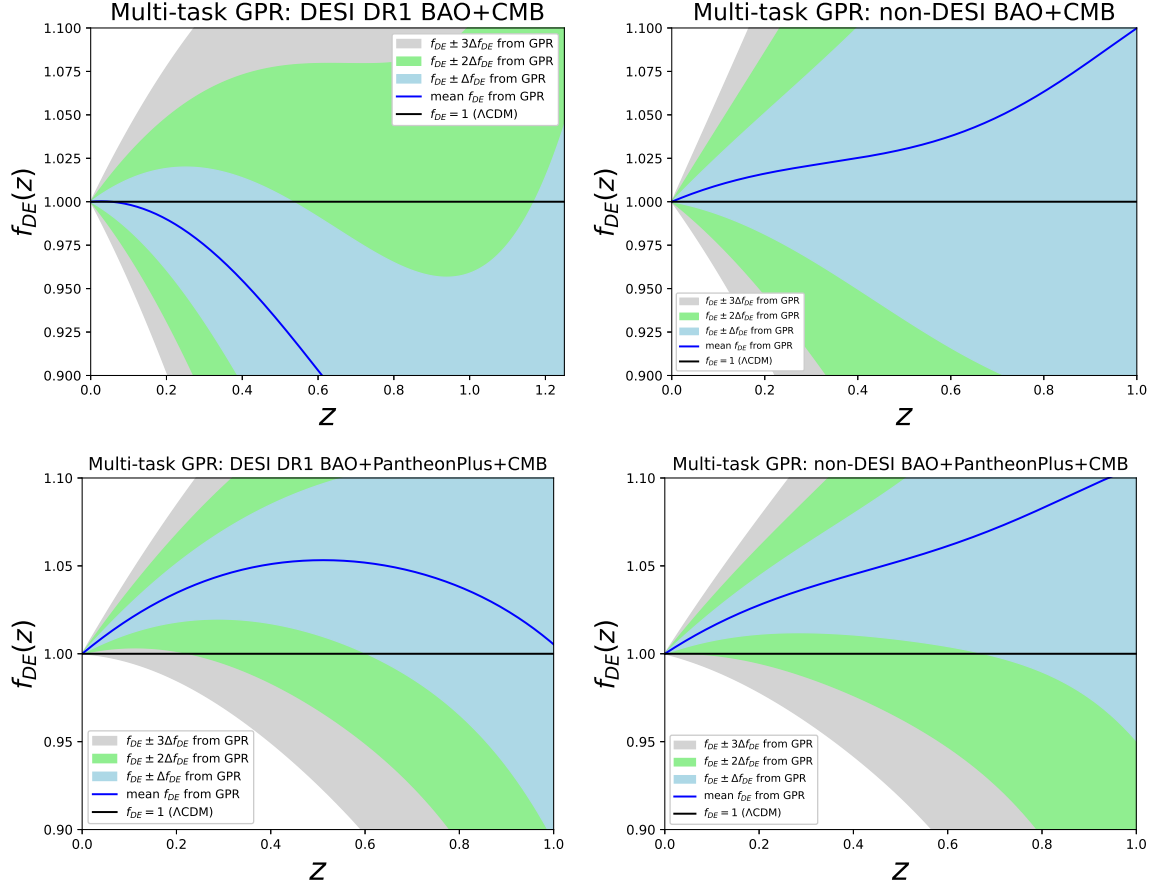


Figure 8. Reconstruction of f_{DE} using (4.21) using CMB+DESI DR1 BAO, CMB+non-DESI BAO, CMB+DESI DR1 BAO+PantheonPlus and CMB+non-DESI BAO+PantheonPlus data. Blue lines are the mean values of f_{DE} obtained from multi-task GPR analysis. Confidence regions correspond to 1σ , 2σ , and 3σ . Horizontal black lines correspond to ΛCDM .

For the ΛCDM model, $f_{\text{DE},\Lambda\text{CDM}} = 1$. Using (2.1) and (2.6),

$$f_{\text{DE}}(z) = \frac{H^2(z) - \alpha(1+z)^3}{H_0^2 - \alpha}. \quad (4.21)$$

This allows us to rewrite f_{DE} in terms of the other variables used in our analysis. Figure 8 shows the reconstructed function f_{DE} for the datasets

CMB+DESI DR1 BAO, CMB+non-DESI BAO,

CMB+DESI DR1 BAO+PantheonPlus, CMB+non-DESI BAO+PantheonPlus.

Solid blue lines give the reconstructed mean f_{DE} . The blue, green (including blue), and gray (including blue and green) regions correspond to 1σ , 2σ , and 3σ confidence regions. Horizontal black lines represent $f_{\text{DE}} = 1$, corresponding to the standard ΛCDM model.

- For the CMB+DESI DR1 BAO combination of data, we find that the ΛCDM model is little more than 1σ away in the redshift range $0.6 \lesssim z \lesssim 1.15$. In other redshift regions, it is well within the 1σ region. This means there are no significant deviations from the ΛCDM model in the CMB+DESI DR1 BAO data combination.

- For the CMB+DESI DR1 BAO+PantheonPlus combination of data, we find that in $z \lesssim 0.2$ the Λ CDM model is little more than 2σ away. In $0.2 \lesssim z \lesssim 0.6$, the Λ CDM model is around 2σ to 1σ away (gradually decreasing with increasing redshift). In other redshift regions, it is within the 1σ limit. This means that the deviations are low to moderate, but not very significant.
- For the CMB+non-DESI BAO combination of data, the Λ CDM model is well within the 1σ region in the entire redshift region. This means there is no evidence for the deviations from the Λ CDM model.
- For the CMB+non-DESI BAO+PantheonPlus combination of data, the Λ CDM model is little more than 1σ away in the redshift range around $0 < z < 0.6$ and it is well within the 1σ region in the other redshift regions. This means for this combination of data the deviations from the Λ CDM model are mild.

4.7 Hubble tension, M_B tension and their connection to w

Table 3 reveals interesting correlations between H_0 , M_B , and Ω_{m0} which bear the Hubble tension and the related M_B tension. This tension is the disagreement between the direct low-redshift measurement from SNIa and the indirect measurement from the CMB.

- The reconstructed H_0 values, where no SHOES data is involved or the corresponding M_B value (≈ -19.25) is not considered, are lower than the $H_0 \approx 73$ obtained via the SHOES data from the calibration of SNIa and observations of Cepheid variables. This is the well-established Hubble tension [89–91].
- A similar conclusion is applicable for M_B , corresponding to the M_B tension [92–94].
- We see that the higher the value of H_0 , the higher the value of M_B , and vice-versa when SNIa data is involved. It is also apparent in Table 4 in Appendix D.3. This is a well-known fact in cosmology [92–94].
- We do not find any immediate connection between H_0 and w when SNIa data are not involved. However, when SNIa (PantheonPlus) data is involved, we see a higher H_0 , corresponding to the higher value of w at lower redshift. The same applies to the correlation between M_B and w . Similarly, the inverse relation applies between Ω_{m0} and w at lower redshift when SNIa data is involved.
- There is an inverse correlation between H_0 and Ω_{m0} , when CMB data is involved (with or without SNIa) [95, 96]. The same inverse correlation exists between M_B and Ω_{m0} when SNIa data is involved. This can also be seen in Table 4 in Appendix D.3. This is also a well-known fact in cosmology.

5 Conclusions

Recent results from DESI DR1 BAO data [1] suggest evidence for dynamical dark energy, with a preference for phantom behaviour in significant redshift ranges. These results rely on a phenomenological parametrised equation of state w for dark energy (or effective dark energy). Given the limitations of imposing such an equation of state, we used a model-agnostic approach to reconstruct $w(z)$ directly from the data.

In addition to the DESI DR1 BAO data, we considered other non-DESI BAO data, CMB distance data from Planck 2018, and SNIa data from PantheonPlus. The model-agnostic methodology is based on the simple (single-task) posterior Gaussian Process regression as well as the multi-task GP regression. Multi-task GP is required to correctly incorporate the correlation between anisotropic BAO observables parallel and perpendicular to the line of sight.

From the CMB+DESI DR1 BAO combination data (see Fig. 3), we find that the reconstructed mean function w is on the phantom side; however, this evidence is not significant. To be more specific, in the redshift range $0.3 \lesssim z \lesssim 0.8$, the Λ CDM model is little more than 1σ away, while in other redshift interval it is well within 1σ limit.

In Fig. 6, when we consider SNIa data from PantheonPlus, the low redshift reconstruction of w is dominated by this data, which has a preference for non-phantom behaviour. The CMB+DESI DR1 BAO+PantheonPlus data leads to a reconstructed w that is not in tension with Λ CDM model – which is $\lesssim 2\sigma$ to 1σ away in the redshift range $z \lesssim 0.35$.

When we replace the DESI DR1 BAO data with the previous non-DESI BAO data, using the combinations CMB+non-DESI BAO (Fig. 4) and CMB+non-DESI BAO+PantheonPlus (Fig. 7), we find no evidence for deviation from the Λ CDM model, which are within the 1σ and 2σ limits respectively.

We also compute constraints on different constants involved in a cosmological analysis, such as the Hubble constant and the present value of the matter energy density parameter. These constraints reflect the Hubble tension and the corresponding M_B tension. When SNIa data are used, we note a higher H_0 together with a corresponding higher w at low redshift.

Finally, we reconstruct the normalised energy density parameter of dark energy, f_{DE} , as a probe to check the consistency of the Λ CDM model against all these observations in Fig. 8. We find a similar conclusion: the deviations from the Λ CDM value ($f_{\text{DE}} = 1$) are not very significant.

Note that all these results use CMB distance priors, which are obtained from the standard base Λ CDM model instead of the full CMB likelihood. The results would be similar for other models of cosmology, provided that the considered model does not differ significantly from the base Λ CDM model.

In summary, our model-agnostic approach suggests significantly low evidence for dynamical dark energy and this evidence is not strong enough to firmly conclude that there is evidence for dynamical dark energy.

Acknowledgments

The authors are supported by the South African Radio Astronomy Observatory and the National Research Foundation (Grant No. 75415).

A Computation of $r_s(z_*)$ and r_d from CMB distance priors

The sound horizon is

$$r_s(z) = \int_z^\infty \frac{c_s(\tilde{z})}{H(\tilde{z})} d\tilde{z} = \int_0^{1/(1+z)} \frac{c_s(a)}{a^2 H(a)} da. \quad (\text{A.1})$$

For early times

$$c_s^2(a) = \frac{c^2}{3[1 + 3\omega_{\text{b}0}/(4\omega_{\gamma 0})a]}, \quad (\text{A.2})$$

where $\omega_{\gamma 0} = \Omega_{\gamma 0} h^2$ and $\Omega_{\gamma 0}$ is the present value of the photon energy density parameter. At sufficiently early times of our interest, the Hubble parameter can be approximated by

$$H^2(z) \approx H_0^2 [\Omega_{\text{m}0}(1+z)^3 + \Omega_{\text{r}0}(1+z)^4], \quad (\text{A.3})$$

where $\Omega_{\text{r}0}$ is the present value of the radiation energy density parameter. In this approximation, the sound horizon is [25]

$$r_s(z) = \tilde{\delta} \log \left\{ \frac{2 + (1+z)(\tilde{\alpha} + \tilde{\gamma}) + 2[(1+z)^2 \tilde{\alpha} \tilde{\gamma} + (1+z)(\tilde{\alpha} + \tilde{\gamma}) + 1]^{1/2}}{(1+z)[\tilde{\alpha} + \tilde{\gamma} + 2(\tilde{\alpha} \tilde{\gamma})^{1/2}]} \right\}, \quad (\text{A.4})$$

where [25, 76–79]

$$\tilde{\alpha} = \frac{\tilde{\beta}}{\omega_{\text{b}0}}, \quad (\text{A.5})$$

$$\tilde{\beta} = \frac{4\omega_{\gamma 0}}{3} = \frac{\theta^4}{31500}, \quad (\text{A.6})$$

$$\theta = \frac{T_{\text{cmb}}}{2.7 \text{ K}}, \quad (\text{A.7})$$

$$\tilde{\gamma} = \frac{\Omega_{\text{r}0}}{\Omega_{\text{m}0}} = \frac{1}{1 + z_{\text{eq}}}, \quad (\text{A.8})$$

$$\tilde{\delta} = \frac{3000 \tilde{\beta}^{1/2}}{(3\omega_{\text{m}0}\omega_{\text{b}0})^{1/2}} \text{ Mpc}. \quad (\text{A.9})$$

Here $T_{\text{cmb}} = 2.7255 \text{ K}$ and z_{eq} is at radiation-matter equality [25, 76–79]:

$$z_{\text{eq}} = 25000 \omega_{\text{m}0} \theta^{-4} \approx 24077.44059 \omega_{\text{m}0}. \quad (\text{A.10})$$

The redshift of the photon decoupling epoch z_* has an approximate expression for standard early time physics [25, 76–79]:

$$z_* = 1048 (1 + 0.00124\omega_{\text{b}0}^{-0.738}) (1 + g_1\omega_{\text{m}0}^{g_2}), \quad (\text{A.11})$$

where

$$g_1 = \frac{0.0783 \omega_{\text{b}0}^{-0.238}}{1 + 39.5 \omega_{\text{b}0}^{0.763}}, \quad (\text{A.12})$$

$$g_2 = \frac{0.560}{1 + 21.1 \omega_{\text{b}0}^{1.81}}. \quad (\text{A.13})$$

Similarly, the redshift of the baryon drag epoch z_d has an approximate expression in standard early time physics [76]:

$$z_d = \frac{1345 \omega_{m0}^{0.251} (1 + b_1 \omega_{b0}^{b_2})}{1 + 0.659 \omega_{m0}^{0.828}}, \quad (\text{A.14})$$

where

$$b_1 = 0.313 \omega_{m0}^{-0.419} (1 + 0.607 \omega_{m0}^{0.674}), \quad (\text{A.15})$$

$$b_2 = 0.238 \omega_{m0}^{0.223}. \quad (\text{A.16})$$

Considering all the above expressions, we find that both $r_s(z_*)$ and r_d are functions of only ω_{m0} and ω_{b0} .

B Gaussian Process Regression

B.1 Single-task Gaussian Process regression up to second order derivative

Gaussian process regression (GPR) analysis is useful to predict a smooth function from a given data set. Let us denote vectors of data points and the observed values of any observable by X_1 and $Y_1 = Y(X_1)$ respectively with the observational errors denoted by a matrix C_{11} corresponding to all the variances and covariances. GPR is only useful if these errors are Gaussian. With this condition, in GPR analysis, data sets are considered to be a multivariate Gaussian (normal) distribution with a specified kernel covariance function K and a mean function μ :

$$Y_1 = Y(X_1) \sim \mathcal{N}(\mu_1, \Sigma_{11}), \quad (\text{B.1})$$

where \mathcal{N} is a joint multivariate Gaussian distribution, μ_1 is the mean vector corresponding to the chosen mean function at X_1 and Σ_{11} is the total covariance matrix:

$$\mu_1 = \mu(X_1), \quad (\text{B.2})$$

$$\Sigma_{11} = K_{11} + C_{11}, \quad (\text{B.3})$$

$$K_{11} = K(X_1, X_1), \quad (\text{B.4})$$

$$C_{11} = \text{Cov}[Y_1, Y_1] = \text{Cov}[Y(X_1), Y(X_1)] \text{ (from observational errors)}. \quad (\text{B.5})$$

The exact vector form of μ_1 and the matrix forms of C_{11} and K_{11} are given in Appendix C.

B.1.1 Training the single-task GPR

Before any prediction from GPR, in a posterior approach, it is trained by minimizing the negative of the logarithmic marginal likelihood

$$-\log P(Y_1|X_1) = \frac{1}{2}(Y_1 - \mu_1)^T \Sigma_{11}^{-1} (Y_1 - \mu_1) + \frac{1}{2} \log |\Sigma_{11}| + \frac{n_1}{2} \log(2\pi), \quad (\text{B.6})$$

where n_1 is the total number of data points, and the notation $|A|$ represents the determinant of any matrix A . We use this notation for the determinant throughout this analysis. The kernel covariance function is described by the kernel hyper-parameters, and best-fit values of these parameters are obtained from the minimisation of the negative log marginal likelihood, mentioned above.

B.1.2 Prediction from single-task GPR

The best-fit values, obtained from the minimization of the negative log marginal likelihood, mentioned in (B.6), are used for the prediction of the function or the function values at a specific target set of points. The predicted values of the function and its derivatives can be considered to be a joint multivariate Gaussian distribution with the observed data. The distribution up to the second-order derivative prediction of the function is

$$\begin{bmatrix} Y_1 \\ F_* \\ F'_* \\ F''_* \end{bmatrix} \sim \mathcal{N} \left(\begin{bmatrix} \mu_1 \\ \mu_* \\ \mu'_* \\ \mu''_* \end{bmatrix}, \begin{bmatrix} \Sigma_{11} & K_{1*} & K_{1*}^{(0,1)} & K_{1*}^{(0,2)} \\ K_{*1} & K_{**} & K_{**}^{(0,1)} & K_{**}^{(0,2)} \\ K_{*1}^{(1,0)} & K_{**}^{(1,0)} & K_{**}^{(1,1)} & K_{**}^{(1,2)} \\ K_{*1}^{(2,0)} & K_{**}^{(2,0)} & K_{**}^{(2,1)} & K_{**}^{(2,2)} \end{bmatrix} \right), \quad (\text{B.7})$$

where subscript '*' corresponds to the target points X_* where GPR predicts the values of a function and its derivatives. All the short notations used above are standard. To have ideas of these short notations, we list this in Appendix C. The predictions of GPR are based on the conditional distributions corresponding to the joint probability distribution of $Y_*^{(p)}$ (for $F_* = Y(X_*)$, $F'_* = Y'(X_*)$, and $F''_* = Y''(X_*)$) given Y_1 and Σ_{11} . These can be easily seen if we rewrite the joint distribution (B.7) as

$$\begin{bmatrix} Y_1 \\ Y_*^{(p)} \end{bmatrix} \sim \mathcal{N} \left(\begin{bmatrix} \mu_1 \\ \mu_*^{(p)} \end{bmatrix}, \begin{bmatrix} \Sigma_{11} & \Sigma_{1*}^{(0,p)} \\ \Sigma_{*1}^{(p,0)} & \Sigma_{**}^{(p,p)} \end{bmatrix} \right), \quad (\text{B.8})$$

where

$$Y_*^{(p)} = \begin{bmatrix} F_* = Y(X_*) \\ F'_* = Y'(X_*) \\ F''_* = Y''(X_*) \end{bmatrix}, \quad \mu_*^{(p)} = \begin{bmatrix} \mu_* = \mu(X_*) \\ \mu'_* = \mu'(X_*) \\ \mu''_* = \mu''(X_*) \end{bmatrix}, \quad (\text{B.9})$$

$$\Sigma_{1*}^{(0,p)} = \begin{bmatrix} K_{1*} & K_{1*}^{(0,1)} & K_{1*}^{(0,2)} \end{bmatrix}, \quad (\text{B.10})$$

$$\begin{aligned} \Sigma_{*1}^{(p,0)} &= \begin{bmatrix} K_{*1} \\ K_{*1}^{(0,1)} \\ K_{*1}^{(0,2)} \end{bmatrix} = \begin{bmatrix} K_{*1}^T & (K_{*1}^{(0,1)})^T & (K_{*1}^{(0,2)})^T \end{bmatrix}^T \\ &= \left(\begin{bmatrix} K_{1*} & K_{1*}^{(1,0)} & K_{1*}^{(2,0)} \end{bmatrix} \right)^T = \left(\Sigma_{1*}^{(0,p)} \right)^T, \end{aligned} \quad (\text{B.11})$$

$$\Sigma_{**}^{(p,p)} = \begin{bmatrix} K_{**} & K_{**}^{(0,1)} & K_{**}^{(0,2)} \\ K_{**}^{(1,0)} & K_{**}^{(1,1)} & K_{**}^{(1,2)} \\ K_{**}^{(2,0)} & K_{**}^{(2,1)} & K_{**}^{(2,2)} \end{bmatrix}. \quad (\text{B.12})$$

Note that one can consider F_* , F'_* , and F''_* separately for a conditional distribution to find mean values and self-covariances of each quantity, but this can not give a prediction for cross covariances. The results would be the same for mean and self-covariances. The conditional distribution for the prediction of Y_*^p given Y_1 corresponding to the Gaussian joint distribution in the form given in (B.8) becomes

$$\bar{Y}_*^{(p)} = \mu_*^{(p)} + \Sigma_{*1}^{(p,0)} \Sigma_{11}^{-1} (Y_1 - \mu_1), \quad (\text{B.13})$$

$$\text{Cov}[Y_*^{(p)}, Y_*^{(p)}] = \Sigma_{**}^{(p,p)} - \Sigma_{*1}^{(p,0)} \Sigma_{11}^{-1} \Sigma_{1*}^{(0,p)}, \quad (\text{B.14})$$

where $\bar{Y}_*^{(p)}$ and $\text{Cov}[Y_*^{(p)}, Y_*^{(p)}]$ are predicted mean (vector) and covariance (matrix) respectively. Throughout this analysis, the overbar on any quantity denotes the mean of the quantity. Putting the corresponding expressions of (B.9) and (B.11) in (B.13), we get the predicted mean of the function and its derivatives at target points:

$$\bar{F}_* = \mu_* + K_{*1} \Sigma_{11}^{-1} (Y_1 - \mu_1), \quad (\text{B.15})$$

$$\bar{F}'_* = \mu'_* + K_{*1}^{(1,0)} \Sigma_{11}^{-1} (Y_1 - \mu_1), \quad (\text{B.16})$$

$$\bar{F}''_* = \mu''_* + K_{*1}^{(2,0)} \Sigma_{11}^{-1} (Y_1 - \mu_1). \quad (\text{B.17})$$

The above three equations can be combined as

$$\bar{F}_*^{(u)} = \mu_*^{(u)} + K_{*1}^{(u,0)} \Sigma_{11}^{-1} (Y_1 - \mu_1), \quad (\text{B.18})$$

where superscript u is the order of the derivative. The above general expression can also be used for the prediction of mean values of the third and higher-order derivatives. Putting the corresponding expressions of (B.10), (B.11), and (B.12) in (B.14), we get the predicted self-covariances,

$$\text{Cov}[F_*, F_*] = K_{**} - K_{*1} \Sigma_{11}^{-1} K_{1*}, \quad (\text{B.19})$$

$$\text{Cov}[F'_*, F'_*] = K_{**}^{(1,1)} - K_{*1}^{(1,0)} \Sigma_{11}^{-1} K_{1*}^{(0,1)}, \quad (\text{B.20})$$

$$\text{Cov}[F''_*, F''_*] = K_{**}^{(2,2)} - K_{*1}^{(2,0)} \Sigma_{11}^{-1} K_{1*}^{(0,2)}. \quad (\text{B.21})$$

Similarly, using (B.10)–(B.12) in (B.14), we find the cross covariances:

$$\text{Cov}[F_*, F'_*] = K_{**}^{(0,1)} - K_{*1} \Sigma_{11}^{-1} K_{1*}^{(0,1)}, \quad (\text{B.22})$$

$$\text{Cov}[F_*, F''_*] = K_{**}^{(0,2)} - K_{*1} \Sigma_{11}^{-1} K_{1*}^{(0,2)}, \quad (\text{B.23})$$

$$\text{Cov}[F'_*, F''_*] = K_{**}^{(1,2)} - K_{*1}^{(1,0)} \Sigma_{11}^{-1} K_{1*}^{(0,2)}. \quad (\text{B.24})$$

The above six equations can be written as

$$\text{Cov}[F_*^{(u)}, F_*^{(v)}] = K_{**}^{(u,v)} - K_{*1}^{(u,0)} \Sigma_{11}^{-1} K_{1*}^{(0,v)}, \quad (\text{B.25})$$

This general expression can be used for third and higher-order order derivatives as well.

B.2 Multi-task GP regression up to second-order derivative

The main aim of this analysis is to use GPR in BAO observations. Because there are large covariances between \tilde{D}_M and \tilde{D}_H , we should not apply simple GPR to each of them separately. For this purpose, we consider multi-task GPR in which the information of function ($Y_1 = Y(X_1)$) and its first derivative ($Y'_2 = Y'(X_2)$) is considered simultaneously at data points X_1 and X_2 respectively. Note that, in the BAO data set the function and its derivative are in the same data points, but here for generality of the methodology, we consider X_1 and X_2 to be different in general (the subset can be the same data points). In this case, we assume that $Y_1 = Y(X_1)$ and $Y'_2 = Y'(X_2)$ follow a joint-multivariate Gaussian distribution

$$\tilde{Y}_1 \sim \mathcal{N}(\tilde{\mu}_1, \tilde{\Sigma}_{11}), \quad (\text{B.26})$$

where \tilde{Y}_1 is the joint vector consisting of vector Y_1 followed by vector Y_2' , $\tilde{\mu}_1$ is the joint vector consisting of vector μ_1 followed by vector μ_2' , and $\tilde{\Sigma}_{11}$ is the joint block matrix consisting of matrices Σ_{11} , $\Sigma_{12}^{(0,1)}$, $\Sigma_{21}^{(1,0)}$, and $\Sigma_{22}^{(1,1)}$:

$$\tilde{Y}_1 = \begin{bmatrix} Y_1 \\ Y_2' \end{bmatrix} = \begin{bmatrix} Y(X_1) \\ Y'(X_2) \end{bmatrix}, \quad (\text{B.27})$$

$$\tilde{\mu}_1 = \begin{bmatrix} \mu_1 \\ \mu_2' \end{bmatrix} = \begin{bmatrix} \mu(X_1) \\ \mu'(X_2) \end{bmatrix}, \quad (\text{B.28})$$

$$\tilde{\Sigma}_{11} = \begin{bmatrix} \Sigma_{11} & \Sigma_{12}^{(0,1)} \\ \Sigma_{21}^{(1,0)} & \Sigma_{22}^{(1,1)} \end{bmatrix}, \quad (\text{B.29})$$

In (B.29), Σ_{11} , $\Sigma_{12}^{(0,1)}$, $\Sigma_{21}^{(1,0)}$, and $\Sigma_{22}^{(1,1)}$ correspond to the total self covariances of Y_1 , total cross covariances between Y_1 and Y_2' , total cross covariances between Y_2' and Y_1 , and total self covariances of Y_2' :

$$\Sigma_{11} = K_{11} + C_{11} \quad \text{-- as in (B.3)}, \quad (\text{B.30})$$

$$\Sigma_{12}^{(0,1)} = K_{12}^{(0,1)} + C_{12}^{(0,1)}, \quad (\text{B.31})$$

$$\Sigma_{21}^{(1,0)} = K_{21}^{(1,0)} + C_{21}^{(1,0)} = \left(K_{12}^{(0,1)}\right)^T + \left(C_{12}^{(0,1)}\right)^T = \left(K_{12}^{(0,1)} + C_{12}^{(0,1)}\right)^T = \left(\Sigma_{12}^{(0,1)}\right)^T, \quad (\text{B.32})$$

$$\Sigma_{22}^{(1,1)} = K_{22}^{(1,1)} + C_{22}^{(1,1)}. \quad (\text{B.33})$$

Here C_{11} , $C_{12}^{(0,1)}$, $C_{21}^{(1,0)}$, and $C_{22}^{(1,1)}$ are the self covariances of Y_1 , cross covariances between Y_1 and Y_2' , cross covariances between Y_2' and Y_1 , and self covariances of Y_2' respectively, corresponding to the contribution only from the observational errors. The actual matrix forms of these matrices are given in Appendix C.

B.2.1 Training the multi-task GPR

Similar to the previous case, here also the GPR is trained by minimizing

$$-\log P(\tilde{Y}_1|\tilde{X}_1) = \frac{1}{2}(\tilde{Y}_1 - \tilde{\mu}_1)^T \tilde{\Sigma}_{11}^{-1}(\tilde{Y}_1 - \tilde{\mu}_1) + \frac{1}{2} \log |\tilde{\Sigma}_{11}| + \frac{\tilde{n}_1}{2} \log(2\pi), \quad (\text{B.34})$$

where \tilde{X}_1 is the joint data points vector consisting of vector X_1 followed by the vector X_2 and \tilde{n}_1 is the total number of data points in the observations corresponding to the function and its first derivative. Then the dimension of the vector \tilde{X}_1 is

$$\tilde{n}_1 = n_1 + n_2. \quad (\text{B.35})$$

The inverse of block matrix $\tilde{\Sigma}_{11}$ can be represented by its constituent matrices:

$$\tilde{\Sigma}_{11}^{-1} = \begin{bmatrix} A_{11} & A_{12} \\ A_{21} & A_{22} \end{bmatrix}, \quad (\text{B.36})$$

where

$$A_{11} = \Sigma_{11}^{-1} + \Sigma_{11}^{-1} \Sigma_{12}^{(0,1)} S \Sigma_{21}^{(1,0)} \Sigma_{11}^{-1}, \quad (\text{B.37})$$

$$A_{12} = -\Sigma_{11}^{-1} \Sigma_{12}^{(0,1)} S, \quad (\text{B.38})$$

$$A_{21} = -S \Sigma_{21}^{(1,0)} \Sigma_{11}^{-1} = A_{12}^T, \quad (\text{B.39})$$

$$A_{22} = S = \left(\Sigma_{22}^{(1,1)} - \Sigma_{21}^{(1,0)} \Sigma_{11}^{-1} \Sigma_{12}^{(0,1)}\right)^{-1}. \quad (\text{B.40})$$

The combination $\tilde{\Sigma}_{11}^{-1}(\tilde{Y}_1 - \tilde{\mu}_1)$ is a vector:

$$\tilde{\Sigma}_{11}^{-1}(\tilde{Y}_1 - \tilde{\mu}_1) = \begin{bmatrix} B_1 \\ B_2 \end{bmatrix}, \quad (\text{B.41})$$

$$B_1 = A_{11}(Y_1 - \mu_1) + A_{12}(Y_2' - \mu_2'), \quad (\text{B.42})$$

$$B_2 = A_{21}(Y_1 - \mu_1) + A_{22}(Y_2' - \mu_2'). \quad (\text{B.43})$$

The combination $(\tilde{Y}_1 - \tilde{\mu}_1)^T \tilde{\Sigma}_{11}^{-1}(\tilde{Y}_1 - \tilde{\mu}_1)$ is a scalar:

$$(\tilde{Y}_1 - \tilde{\mu}_1)^T \tilde{\Sigma}_{11}^{-1}(\tilde{Y}_1 - \tilde{\mu}_1) = (Y_1 - \mu_1)^T B_1 + (Y_2' - \mu_2')^T B_2 \equiv Q. \quad (\text{B.44})$$

The determinant of the block matrix $\tilde{\Sigma}_{11}$ can be expressed by the determinants of its constituent matrices,

$$|\tilde{\Sigma}_{11}| = |\Sigma_{11}| |\Sigma_{22}^{(1,1)} - \Sigma_{21}^{(1,0)} \Sigma_{11}^{-1} \Sigma_{12}^{(0,1)}| = |\Sigma_{11}| |S^{-1}| = \frac{|\Sigma_{11}|}{|S|}. \quad (\text{B.45})$$

Putting (B.35), (B.44) and (B.45) into (B.34), we have

$$-\log P(\tilde{Y}|\tilde{X}) = \frac{1}{2} \left[Q + \log |\Sigma_{11}| - \log |S| + (n_1 + n_2) \log(2\pi) \right]. \quad (\text{B.46})$$

B.2.2 Prediction from multi-task GPR

The observed data of the main function $Y_1 = Y(X_1)$ and its derivative $Y_2' = Y'(X_2)$ and the predicted values of the function and its derivatives can be represented by a joint-multivariate Gaussian distribution:

$$\begin{bmatrix} Y_1 \\ Y_2' \\ F_* \\ F_*' \\ F_*'' \end{bmatrix} \sim \mathcal{N} \left(\begin{bmatrix} \mu_1 \\ \mu_2' \\ \mu_* \\ \mu_*' \\ \mu_*'' \end{bmatrix}, \begin{bmatrix} \Sigma_{11} & \Sigma_{12}^{(0,1)} & K_{1*} & K_{1*}^{(0,1)} & K_{1*}^{(0,2)} \\ \Sigma_{21}^{(1,0)} & \Sigma_{22}^{(1,1)} & K_{2*}^{(1,0)} & K_{2*}^{(1,1)} & K_{2*}^{(1,2)} \\ K_{*1} & K_{*2}^{(0,1)} & K_{**} & K_{**}^{(0,1)} & K_{**}^{(0,2)} \\ K_{*1}^{(1,0)} & K_{*2}^{(1,1)} & K_{**}^{(1,0)} & K_{**}^{(1,1)} & K_{**}^{(1,2)} \\ K_{*1}^{(2,0)} & K_{*2}^{(2,1)} & K_{**}^{(2,0)} & K_{**}^{(2,1)} & K_{**}^{(2,2)} \end{bmatrix} \right). \quad (\text{B.47})$$

Here the notations are standard for all the vectors and matrices and these are given in Appendix C. This distribution can be rewritten in a form equivalent to the form in (B.7) using definitions of \tilde{Y}_1 , $\tilde{\mu}_1$, and $\tilde{\Sigma}_{11}$ from (B.27)–(B.29):

$$\begin{bmatrix} \tilde{Y}_1 \\ F_* \\ F_*' \\ F_*'' \end{bmatrix} \sim \mathcal{N} \left(\begin{bmatrix} \tilde{\mu}_1 \\ \mu_* \\ \mu_*' \\ \mu_*'' \end{bmatrix}, \begin{bmatrix} \tilde{\Sigma}_{11} & \tilde{K}_{1*} & \tilde{K}_{1*}^{(0,1)} & \tilde{K}_{1*}^{(0,2)} \\ \tilde{K}_{*1} & K_{**} & K_{**}^{(0,1)} & K_{**}^{(0,2)} \\ \tilde{K}_{*1}^{(1,0)} & K_{**}^{(1,0)} & K_{**}^{(1,1)} & K_{**}^{(1,2)} \\ \tilde{K}_{*1}^{(2,0)} & K_{**}^{(2,0)} & K_{**}^{(2,1)} & K_{**}^{(2,2)} \end{bmatrix} \right). \quad (\text{B.48})$$

Here

$$\tilde{K}_{1*} = \begin{bmatrix} K_{1*} \\ K_{2*}^{(1,0)} \end{bmatrix}, \quad (\text{B.49})$$

$$\tilde{K}_{1*}^{(0,1)} = \begin{bmatrix} K_{1*}^{(0,1)} \\ K_{2*}^{(1,1)} \end{bmatrix}, \quad (\text{B.50})$$

$$\tilde{K}_{1*}^{(0,2)} = \begin{bmatrix} K_{1*}^{(0,2)} \\ K_{2*}^{(1,2)} \end{bmatrix}. \quad (\text{B.51})$$

Similarly,

$$\tilde{K}_{*1} = \begin{bmatrix} K_{*1} & K_{*2}^{(0,1)} \end{bmatrix} = \begin{bmatrix} K_{*1}^T \\ \left(K_{*2}^{(0,1)}\right)^T \end{bmatrix}^T = \begin{bmatrix} K_{1*} \\ K_{2*}^{(1,0)} \end{bmatrix}^T = \tilde{K}_{1*}^T, \quad (\text{B.52})$$

$$\tilde{K}_{*1}^{(1,0)} = \begin{bmatrix} K_{*1}^{(1,0)} & K_{*2}^{(1,1)} \end{bmatrix} = \begin{bmatrix} \left(K_{*1}^{(1,0)}\right)^T \\ \left(K_{*2}^{(1,1)}\right)^T \end{bmatrix}^T = \begin{bmatrix} K_{1*}^{(0,1)} \\ K_{2*}^{(1,1)} \end{bmatrix}^T = \left(\tilde{K}_{1*}^{(0,1)}\right)^T, \quad (\text{B.53})$$

$$\tilde{K}_{*1}^{(2,0)} = \begin{bmatrix} K_{*1}^{(2,0)} & K_{*2}^{(2,1)} \end{bmatrix} = \begin{bmatrix} \left(K_{*1}^{(2,0)}\right)^T \\ \left(K_{*2}^{(2,1)}\right)^T \end{bmatrix}^T = \begin{bmatrix} K_{1*}^{(0,2)} \\ K_{2*}^{(1,2)} \end{bmatrix}^T = \left(\tilde{K}_{1*}^{(0,2)}\right)^T. \quad (\text{B.54})$$

Comparing the same structure between (B.7) and (B.48), we find predictions with the similar structure. For the mean values of the functions and their derivatives:

$$\bar{F}_* = \mu_* + \tilde{K}_{*1} \tilde{\Sigma}_{11}^{-1} (\tilde{Y}_1 - \tilde{\mu}_1) = \mu_* + K_{*1} B_1 + K_{*2}^{(0,1)} B_2, \quad (\text{B.55})$$

$$\bar{F}'_* = \mu'_* + \tilde{K}_{*1}^{(1,0)} \tilde{\Sigma}_{11}^{-1} (\tilde{Y}_1 - \tilde{\mu}_1) = \mu'_* + K_{*1}^{(1,0)} B_1 + K_{*2}^{(1,1)} B_2, \quad (\text{B.56})$$

$$\bar{F}''_* = \mu''_* + \tilde{K}_{*1}^{(2,0)} \tilde{\Sigma}_{11}^{-1} (\tilde{Y}_1 - \tilde{\mu}_1) = \mu''_* + K_{*1}^{(2,0)} B_1 + K_{*2}^{(2,1)} B_2. \quad (\text{B.57})$$

These equations can be written as

$$\bar{F}_*^{(u)} = \mu_*^{(u)} + K_{*1}^{(u,0)} B_1 + K_{*2}^{(u,1)} B_2, \quad (\text{B.58})$$

which can be used for the prediction of mean values of the third and higher-order derivatives too. Similarly, we get the prediction for the self-covariances

$$\begin{aligned} \text{Cov}[F_*, F_*] &= K_{**} - \tilde{K}_{*1} \tilde{\Sigma}_{11}^{-1} \tilde{K}_{1*}, \\ &= K_{**} - K_{*1} \left(A_{11} K_{1*} + A_{12} K_{2*}^{(1,0)} \right) - K_{*2}^{(0,1)} \left(A_{21} K_{1*} + A_{22} K_{2*}^{(1,0)} \right), \end{aligned} \quad (\text{B.59})$$

$$\begin{aligned} \text{Cov}[F'_*, F'_*] &= K_{**}^{(1,1)} - \tilde{K}_{*1}^{(1,0)} \tilde{\Sigma}_{11}^{-1} \tilde{K}_{1*}^{(0,1)}, \\ &= K_{**}^{(1,1)} - K_{*1}^{(1,0)} \left(A_{11} K_{1*}^{(0,1)} + A_{12} K_{2*}^{(1,1)} \right) - K_{*2}^{(1,1)} \left(A_{21} K_{1*}^{(0,1)} + A_{22} K_{2*}^{(1,1)} \right), \end{aligned} \quad (\text{B.60})$$

$$\begin{aligned} \text{Cov}[F''_*, F''_*] &= K_{**}^{(2,2)} - \tilde{K}_{*1}^{(2,0)} \tilde{\Sigma}_{11}^{-1} \tilde{K}_{1*}^{(0,2)}, \\ &= K_{**}^{(2,2)} - K_{*1}^{(2,0)} \left(A_{11} K_{1*}^{(0,2)} + A_{12} K_{2*}^{(1,2)} \right) - K_{*2}^{(2,1)} \left(A_{21} K_{1*}^{(0,2)} + A_{22} K_{2*}^{(1,2)} \right), \end{aligned} \quad (\text{B.61})$$

and for the cross covariances,

$$\begin{aligned} \text{Cov}[F_*, F'_*] &= \text{Cov}[F'_*, F_*]^T = K_{**}^{(0,1)} - \tilde{K}_{*1} \tilde{\Sigma}_{11}^{-1} \tilde{K}_{1*}^{(0,1)}, \\ &= K_{**}^{(0,1)} - K_{*1} \left(A_{11} K_{1*}^{(0,1)} + A_{12} K_{2*}^{(1,1)} \right) - K_{*2}^{(0,1)} \left(A_{21} K_{1*}^{(0,1)} + A_{22} K_{2*}^{(1,1)} \right), \end{aligned} \quad (\text{B.62})$$

$$\begin{aligned} \text{Cov}[F_*, F''_*] &= \text{Cov}[F''_*, F_*]^T = K_{**}^{(0,2)} - \tilde{K}_{*1} \tilde{\Sigma}_{11}^{-1} \tilde{K}_{1*}^{(0,2)}, \\ &= K_{**}^{(0,2)} - K_{*1} \left(A_{11} K_{1*}^{(0,2)} + A_{12} K_{2*}^{(1,2)} \right) - K_{*2}^{(0,1)} \left(A_{21} K_{1*}^{(0,2)} + A_{22} K_{2*}^{(1,2)} \right), \end{aligned} \quad (\text{B.63})$$

$$\begin{aligned} \text{Cov}[F'_*, F''_*] &= \text{Cov}[F''_*, F'_*]^T = K_{**}^{(1,2)} - \tilde{K}_{*1}^{(1,0)} \tilde{\Sigma}_{11}^{-1} \tilde{K}_{1*}^{(0,2)}, \\ &= K_{**}^{(1,2)} - K_{*1}^{(1,0)} \left(A_{11} K_{1*}^{(0,2)} + A_{12} K_{2*}^{(1,2)} \right) - K_{*2}^{(1,1)} \left(A_{21} K_{1*}^{(0,2)} + A_{22} K_{2*}^{(1,2)} \right). \end{aligned} \quad (\text{B.64})$$

The above six equations can be written in the form

$$\begin{aligned} \text{Cov}[F_*^{(u)}, F_*^{(v)}] &= K_{**}^{(u,v)} - K_{*1}^{(u,0)} \left(A_{11} K_{1*}^{(0,v)} + A_{12} K_{2*}^{(1,v)} \right) \\ &\quad - K_{*2}^{(u,1)} \left(A_{21} K_{1*}^{(0,v)} + A_{22} K_{2*}^{(1,v)} \right). \end{aligned} \quad (\text{B.65})$$

This general expression can also be used for third and higher-order derivatives.

B.3 Recovering single-task GPR from multi-task GPR

We can recover the single-task GPR results if we do not have any information from the derivative of the main function $Y_2' = Y'(X_2)$. This can either be done by removing all the quantities which are made up of data in the first derivative of the function or it can be done by quantifying the standard deviation in the derivative of the function corresponding to infinite observational errors, i.e.,

$$\text{each diagonal element of } C_{22}^{(1,1)} \rightarrow \infty, \quad (\text{B.66})$$

Using this in (B.40), we get the zero matrix:

$$S = \{0\}. \quad (\text{B.67})$$

From (B.37)–(B.43),

$$A_{11} = \Sigma_{11}^{-1}, \quad A_{12} = \{0\}, \quad A_{21} = \{0\}, \quad A_{22} = \{0\}, \quad (\text{B.68})$$

$$B_1 = \Sigma_{11}^{-1}(Y_1 - \mu_1), \quad B_2 = \{0\}. \quad (\text{B.69})$$

Then (B.44) gives

$$Q = (Y - \mu)^\top \Sigma_{11}^{-1} (Y_1 - \mu_1). \quad (\text{B.70})$$

Using (B.67) and (B.70) in (B.46), the negative log marginal likelihood becomes

$$-\log P(\tilde{Y}|\tilde{X}) \rightarrow -\log P(Y_1|X_1) + \left[\infty + \frac{n_2}{2} \log(2\pi) \right], \quad (\text{B.71})$$

showing that no constraints come from the derivative information.

Now we can see that if we use (B.69) in (B.55)–(B.58), we recover the standard results of (B.15)–(B.18), where there is no information on the derivative of the function. Similarly, putting conditions of (B.68) in (B.59)–(B.65), we recover the standard results (B.19)–(B.25).

C Notation used in the GPR analysis

Here we list all the short notations which were used in the GPR analysis in the main text. The short notations for vectors are as follows:

$$\begin{aligned}
 X_1 &= \begin{bmatrix} x_1^1 \\ x_1^2 \\ \vdots \\ x_1^{n_1} \end{bmatrix}, \quad Y_1 = Y(X_1) = \begin{bmatrix} y_1^1 = y(x_1^1) \\ y_1^2 = y(x_1^2) \\ \vdots \\ y_1^{n_1} = y(x_1^{n_1}) \end{bmatrix}, \quad X_2 = \begin{bmatrix} x_2^1 \\ x_2^2 \\ \vdots \\ x_2^{n_2} \end{bmatrix}, \quad Y_2' = Y'(X_2) = \begin{bmatrix} y_2'^1 = y'(x_2^1) \\ y_2'^2 = y'(x_2^2) \\ \vdots \\ y_2'^{n_2} = y'(x_2^{n_2}) \end{bmatrix}, \\
 X_* &= \begin{bmatrix} x_*^1 \\ x_*^2 \\ \vdots \\ x_*^m \end{bmatrix}, \quad F_* = Y(X_*) = \begin{bmatrix} f_*^1 = y(x_*^1) \\ f_*^2 = y(x_*^2) \\ \vdots \\ f_*^m = y(x_*^m) \end{bmatrix}, \quad F_*' = Y'(X_*) = \begin{bmatrix} f_*'^1 = y'(x_*^1) \\ f_*'^2 = y'(x_*^2) \\ \vdots \\ f_*'^m = y'(x_*^m) \end{bmatrix}, \quad (C.1)
 \end{aligned}$$

where m is the number of points, where we want the predictions from GPR for the function and its derivatives. Similar to the notations of vectors in (C.1), the same rule applies for the notations of vectors $F_*'' = Y''(X_*)$, $\bar{F}_* = \bar{Y}(X_*)$, $\bar{F}_*' = \bar{Y}'(X_*)$, and $\bar{F}_*'' = \bar{Y}''(X_*)$ of dimension m .

The covariance matrix C_{11} corresponding to the self covariances of the main function $Y_1 = Y(X_1)$ has the matrix form given as

$$\begin{aligned}
 C_{11} &= \text{Cov}[Y_1, Y_1] = \text{Cov}[Y(X_1), Y(X_1)] = \left\{ c_{11}^{ij} \right\} = \left\{ \text{Cov}[y_1^i, y_1^j] \right\} \\
 &= \begin{bmatrix} \text{Cov}[y_1^1, y_1^1] & \text{Cov}[y_1^1, y_1^2] & \dots & \text{Cov}[y_1^1, y_1^{n_1}] \\ \text{Cov}[y_1^2, y_1^1] & \text{Cov}[y_1^2, y_1^2] & \dots & \text{Cov}[y_1^2, y_1^{n_1}] \\ \vdots & \vdots & \dots & \vdots \\ \vdots & \vdots & \dots & \vdots \\ \text{Cov}[y_1^{n_1}, y_1^1] & \text{Cov}[y_1^{n_1}, y_1^2] & \dots & \text{Cov}[y_1^{n_1}, y_1^{n_1}] \end{bmatrix}, \quad (C.2)
 \end{aligned}$$

where i and j run from 1 to n_1 . We shall also consider indices p and q which run from 1 to n_2 and indices r and s which run from 1 to m :

$$i, j \in [1, 2, \dots, n_1], \quad p, q \in [1, 2, \dots, n_2], \quad r, s \in [1, 2, \dots, m]. \quad (C.3)$$

The covariance matrix $C_{12}^{(0,1)}$ corresponding to the cross covariances of the main function $Y_1 = Y(X_1)$ and its derivative $Y_2' = Y'(X_2)$ has the matrix form

$$\begin{aligned}
 C_{12}^{(0,1)} &= \text{Cov}[Y_1, Y_2'] = \text{Cov}[Y(X_1), Y'(X_2)] = \left\{ c_{12}^{(0,1)ip} \right\} = \left\{ \text{Cov}[y_1^i, y_2'^p] \right\} \\
 &= \begin{bmatrix} \text{Cov}[y_1^1, y_2'^1] & \text{Cov}[y_1^1, y_2'^2] & \dots & \text{Cov}[y_1^1, y_2'^{n_2}] \\ \text{Cov}[y_1^2, y_2'^1] & \text{Cov}[y_1^2, y_2'^2] & \dots & \text{Cov}[y_1^2, y_2'^{n_2}] \\ \vdots & \vdots & \dots & \vdots \\ \vdots & \vdots & \dots & \vdots \\ \text{Cov}[y_1^{n_1}, y_2'^1] & \text{Cov}[y_1^{n_1}, y_2'^2] & \dots & \text{Cov}[y_1^{n_1}, y_2'^{n_2}] \end{bmatrix} = \left(C_{21}^{(1,0)} \right)^T. \quad (C.4)
 \end{aligned}$$

The covariance matrix $C_{22}^{(1,1)}$ corresponding to the self covariances of the derivative of the function $Y'_2 = Y'(X_2)$ has the matrix form

$$\begin{aligned}
C_{22}^{(1,1)} &= \text{Cov}[Y'_2, Y'_2] = \text{Cov}[Y'(X_2), Y'(X_2)] = \left\{ c_{22}^{(1,1)pq} \right\} = \left\{ \text{Cov}[y'_2{}^p, y'_2{}^q] \right\} \\
&= \begin{bmatrix} \text{Cov}[y'_2{}^1, y'_2{}^1] & \text{Cov}[y'_2{}^1, y'_2{}^2] & \dots & \text{Cov}[y'_2{}^1, y'_2{}^{n_2}] \\ \text{Cov}[y'_2{}^2, y'_2{}^1] & \text{Cov}[y'_2{}^2, y'_2{}^2] & \dots & \text{Cov}[y'_2{}^2, y'_2{}^{n_2}] \\ \vdots & \vdots & \dots & \vdots \\ \vdots & \vdots & \dots & \vdots \\ \text{Cov}[y'_2{}^{n_2}, y'_2{}^1] & \text{Cov}[y'_2{}^{n_2}, y'_2{}^2] & \dots & \text{Cov}[y'_2{}^{n_2}, y'_2{}^{n_2}] \end{bmatrix}. \tag{C.5}
\end{aligned}$$

The short notations for the other matrices are

$$K_{11} = K(X_1, X_1) = \left\{ k(x_1^i, x_1^j) \right\} = \begin{bmatrix} k(x_1^1, x_1^1) & k(x_1^1, x_1^2) & \dots & k(x_1^1, x_1^{n_1}) \\ k(x_1^2, x_1^1) & k(x_1^2, x_1^2) & \dots & k(x_1^2, x_1^{n_1}) \\ \vdots & \vdots & \dots & \vdots \\ \vdots & \vdots & \dots & \vdots \\ k(x_1^{n_1}, x_1^1) & k(x_1^{n_1}, x_1^2) & \dots & k(x_1^{n_1}, x_1^{n_1}) \end{bmatrix}, \tag{C.6}$$

$$K_{1*} = K(X_1, X_*) = \left\{ k(x_1^i, x_*^r) \right\} = \begin{bmatrix} k(x_1^1, x_*^1) & k(x_1^1, x_*^2) & \dots & k(x_1^1, x_*^m) \\ k(x_1^2, x_*^1) & k(x_1^2, x_*^2) & \dots & k(x_1^2, x_*^m) \\ \vdots & \vdots & \dots & \vdots \\ \vdots & \vdots & \dots & \vdots \\ k(x_1^{n_1}, x_*^1) & k(x_1^{n_1}, x_*^2) & \dots & k(x_1^{n_1}, x_*^m) \end{bmatrix} = K_{*1}^T. \tag{C.7}$$

The same matrix notations are applied to other matrices with the same rules. Some relevant matrix notations are listed below without showing the actual matrix:

$$K_{**} = K(X_*, X_*) = \left\{ k(x_*^r, x_*^s) \right\}, \tag{C.8}$$

$$K_{11}^{(u,v)} = K^{(u,v)}(X_1, X_1) = \left\{ k^{(u,v)}(x_1^i, x_1^j) \right\} = \left\{ \frac{\partial^{(u+v)} k(x_1^i, x_1^j)}{\partial x_1^{i u} \partial x_1^{j v}} \right\}, \tag{C.9}$$

$$K_{1*}^{(u,v)} = K^{(u,v)}(X_1, X_*) = \left\{ k^{(u,v)}(x_1^i, x_*^r) \right\} = \left\{ \frac{\partial^{(u+v)} k(x_1^i, x_*^r)}{\partial x_1^{i u} \partial x_*^{r v}} \right\}, \tag{C.10}$$

$$K_{**}^{(u,v)} = K^{(u,v)}(X_*, X_*) = \left\{ k^{(u,v)}(x_*^r, x_*^s) \right\} = \left\{ \frac{\partial^{(u+v)} k(x_*^r, x_*^s)}{\partial x_*^{r u} \partial x_*^{s v}} \right\}, \tag{C.11}$$

and so on, where u and v are the orders of the differentiation of the kernel with respect to the first and second arguments.

D Application of single-task GPR to PantheonPlus data and role of M_B

D.1 PantheonPlus+SHOES and CMB+PantheonPlus+SHOES

The PantheonPlus dataset (3.17) provides apparent magnitude m_B and also data on distance modulus μ_B , obtained from the calibration with local Cepheid measurements from SHOES

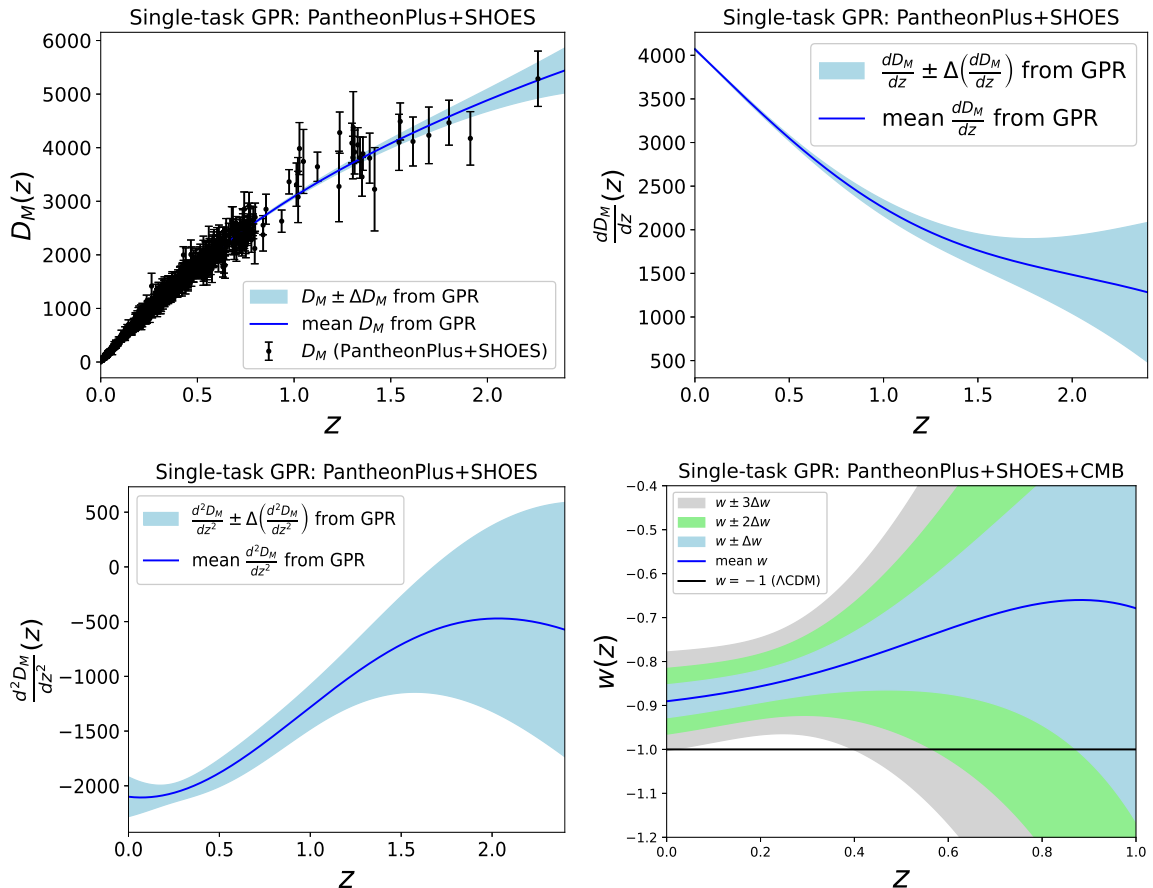


Figure 9. Black error bars in the top left panel give $D_M \pm \Delta D_M$ obtained from observed μ_B of PantheonPlus+SHOES, using (2.14). Solid blue lines and blue shadings in the top left, top right, and bottom left panels correspond to the reconstructed D_M , D'_M , and D''_M , with associated 1σ confidence regions, using single-task GPR. The bottom right panel shows the reconstructed w and associated confidence regions for CMB+PantheonPlus+SHOES (single-task GPR) using (2.9) and (3.15).

observations. When we consider m_B data, we are using only PantheonPlus data. On the other hand, when we consider μ_B data, we are using PantheonPlus and SHOES data together.

We first consider the μ_B data and the associated errors. For this, we consider the full covariance coming from both statistics and systematics. Then we compute D_M using (2.14) and the corresponding error by propagation of uncertainty. These are shown in the top left panel of Fig. 9 with black error bars. We apply the GPR analysis to these D_M data. Unlike BAO data, these data correspond to only one function D_M . So, in this case, single-task GPR is applicable. Applying single-task GPR, we compute predictions for mean values of D_M , its first derivative, and its second derivative using (B.15)–(B.17). We also compute errors using (B.19)–(B.21). The predicted D_M and the associated 1σ confidence interval are shown in the top left panel of Fig. 9 as a blue line and blue shading.

Similarly, we show D'_M and D''_M , together with the associated 1σ confidence intervals, in the top right and bottom left panels of Fig. 9. We then compute cross covariances between D'_M and D''_M using (B.24).

Using the reconstructed D'_M and D''_M , their self-covariances and cross-covariances, we

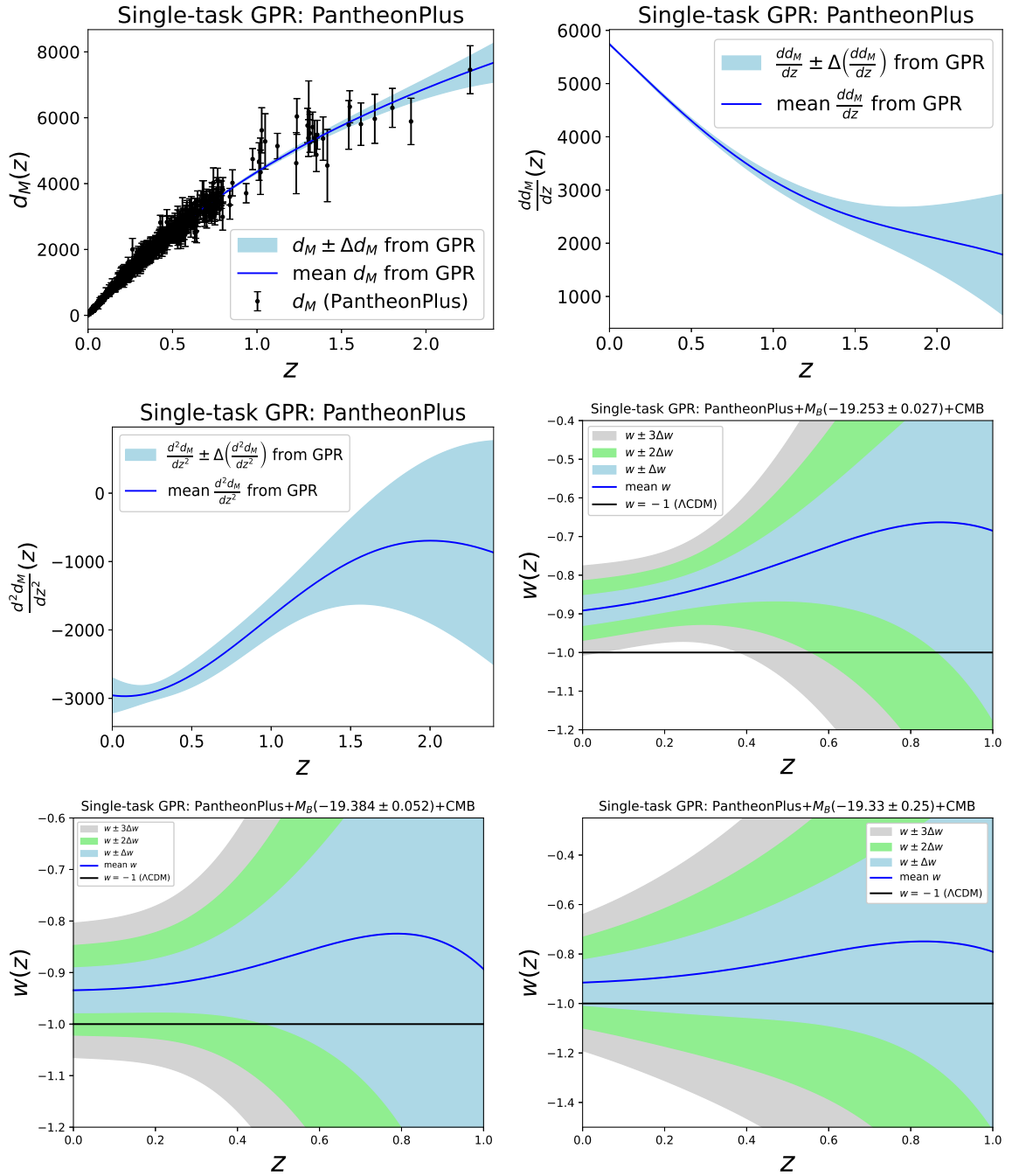


Figure 10. The top panels and the middle left panel show the reconstructed d_M , d_M' , and d_M'' and associated 1σ confidence regions respectively using single-task GPR. Black error bars in the top left panel are from the observed m_B of PantheonPlus data, using (2.15). The remaining three panels show the reconstructed w and associated confidence regions for CMB+PantheonPlus (single-task GPR) with three different M_B Gaussian priors (D.1)–(D.3), using (2.16), (2.17) and (3.15).

compute the redshift evolution of w from (2.9), with the additional CMB information of β in (3.15). The reconstructed w and its errors are displayed in the bottom right panel of Fig. 9,

with the same color codes as in Fig. 3. From this plot, we see that the Λ CDM model is more than 3σ away in the redshift range $0 \lesssim z \lesssim 0.4$, for the CMB+PantheonPlus+SHOES combination of data sets. It is 3σ to 1σ away in the redshift range around $0.4 \lesssim z \lesssim 0.9$. For $z \gtrsim 0.9$ it is well within the 1σ limit. In most of the lower redshift range, the reconstructed w is in the non-phantom region.

D.2 PantheonPlus, PantheonPlus+ M_B and CMB+PantheonPlus+ M_B

It is not essential that we calibrate PantheonPlus data with the SHOES observations. To keep other options open, we combine PantheonPlus data with other data sets. Without calibration with SHOES, we cannot use μ_B data from PantheonPlus. For this case, we consider instead m_B data. Here, also we consider full covariance including systematic errors from PantheonPlus data. From this m_B data, we compute d_M using (2.15) and the associated error using propagation of uncertainty. The result is shown in the top left panel of Fig. 10 with black error bars. We apply single-task GPR to the d_M data in order to predict the smooth function of d_M and its first and second derivatives, and the associated errors (the blue line and shading). We see that the predicted $d_M(z)$ is consistent with the d_M data. The predicted d'_M and d''_M and the associated 1σ confidence intervals are plotted in the top right and middle left panels of Fig. 10.

In order to reconstruct w from the predicted d'_M and d''_M using (2.16), we need values of the parameter δ in (2.17), which involves parameters β and M_B . We use the β value from CMB data, as in (3.15). Additional information on the M_B parameter is needed. For this, we use three significantly different Gaussian priors on M_B [97]:

$$M_B \text{ Prior I: } M_B = -19.253 \pm 0.027, \quad (\text{D.1})$$

$$M_B \text{ Prior II: } M_B = -19.384 \pm 0.052, \quad (\text{D.2})$$

$$M_B \text{ Prior III: } M_B = -19.33 \pm 0.25. \quad (\text{D.3})$$

Prior I is from SHOES, used to cross-check the consistency with the previous result [98]. Prior II is obtained from the calibration of the Pantheon sample with cosmic chronometer observations of the Hubble parameter [99]. Prior III is from 18 SNIa [100] obtained using multicolor light curve shapes [101].

With M_B Prior I, we reconstruct w and the associated error regions, shown in the middle right panel of Fig. 10. Comparing with the bottom right panel of Fig. 9, we see that the results are consistent and the same conclusion is applicable here.

Using M_B Prior II, we reconstruct w and associated confidence regions, shown in the bottom left panel of Fig. 10. In this case, the Λ CDM model is 1.5σ to 1σ away in the redshift range $0 \lesssim z \lesssim 0.45$ and well within 1σ region in the redshift range $z \gtrsim 0.45$.

The M_B Prior III leads to the bottom right panel of Fig. 10. Here we see that Λ CDM is within the 1σ region in the entire redshift range. Note that, at lower redshifts, the reconstructed mean function of w lies within the mean functions corresponding to M_B Prior I and M_B Prior II. This is because the mean value of M_B in Prior III lies within the mean values of Priors I and II. The higher the M_B prior value, the higher the mean value of w in the non-phantom region. The confidence region is largest for M_B Prior III since the error in M_B is largest in this case.

D.3 Extended list of reconstructed constants

$$\text{SNIa}+M_B: H_0 = \frac{c e^{b(20+M_B)}}{d_H(z=0)}, \quad M_B \text{ (provided)}, \quad (\text{D.4})$$

$$\begin{aligned}
\text{CMB+SNIa}+M_B: \quad H_0 &= \frac{c e^{b(20+M_B)}}{d_H(z=0)} \text{ (same as for SNIa}+M_B), \quad H_0 r_d = H_0 \times r_d, \\
\Omega_{m0} &= \frac{\omega_{m0}}{h^2}, \quad M_B \text{ (provided)}.
\end{aligned} \tag{D.5}$$

Data combination	$H_0 r_d$ [100 km/s]	H_0 [km/s/Mpc]	Ω_{m0}	M_B [mag]
PP+ M_B Prior I	-	73.72 ± 0.95	-	-19.253 ± 0.027
PP+ M_B Prior II	-	69.41 ± 1.68	-	-19.384 ± 0.052
PP+ M_B Prior III	-	71.16 ± 8.20	-	-19.33 ± 0.25
CMB+PP+ M_B Prior I	108.40 ± 1.42	73.72 ± 0.95	0.263 ± 0.007	-19.253 ± 0.027
CMB+PP+ M_B Prior II	102.06 ± 2.48	69.41 ± 1.68	0.297 ± 0.015	-19.384 ± 0.052
CMB+PP+ M_B Prior III	104.63 ± 12.05	71.16 ± 8.20	0.282 ± 0.065	-19.33 ± 0.25

Table 4. Extended list of reconstructed values of $H_0 r_d$, H_0 , Ω_{m0} and M_B .

E Dependence on different CMB distance priors

To compute CMB distance priors we used `base_plikHM_TTTEEE_lowl_lowE_lensing` from the Planck data archive with standard Λ CDM [79]. We denote the resulting CMB distance prior CMB(P18 I). Here we check how the results change if we change the CMB distance prior [102, 103]. For the second CMB distance prior, CMB(P18 II), we exclude the constraints from lensing, i.e. we use Planck 2018 TT,TE,EE+lowE, and we assume w CDM instead of Λ CDM. The corresponding CMB distance priors use the chain `base_w_plikHM_TTTEEE_lowl_lowE` with the w CDM model [77]. For the third CMB distance prior, CMB(P18 III), we generalize the early physics of Λ CDM to the varying sum of neutrino masses and varying effective number of relativistic species, in order to get comparatively broader standard deviations in distance priors. For this, we use the chain `base_nnu_mnu_plikHM_TT_lowl_lowE_post_lensing` [78]. We obtain the γ values

$$\gamma = (343.8 \pm 1.6) \times 10^{-6} \quad \text{CMB(P18 I)}, \tag{E.1}$$

$$\gamma = (344.4 \pm 1.9) \times 10^{-6} \quad \text{CMB(P18 II)}, \tag{E.2}$$

$$\gamma = (342.5 \pm 3.1) \times 10^{-6} \quad \text{CMB(P18 III)}. \tag{E.3}$$

The mean values are slightly different in the three cases. CMB(P18 II) has a slightly larger standard deviation than CMB(P18 I), whereas CMB(P18 III) has a significantly larger standard deviation. Figure 11 shows the Gaussian distributions of γ .

In Fig. 12, we plot the dark energy equation of state for DESI DR1 BAO combined with three different CMB distance priors. It is evident that there are no significant differences in w for the three different γ .

Figure 13 repeats the plots in Fig. 12, but with the addition of the PantheonPlus data, i.e. for DESI DR1 BAO+PantheonPlus combined with three different CMB distance priors. Again, we see that the results are similar.

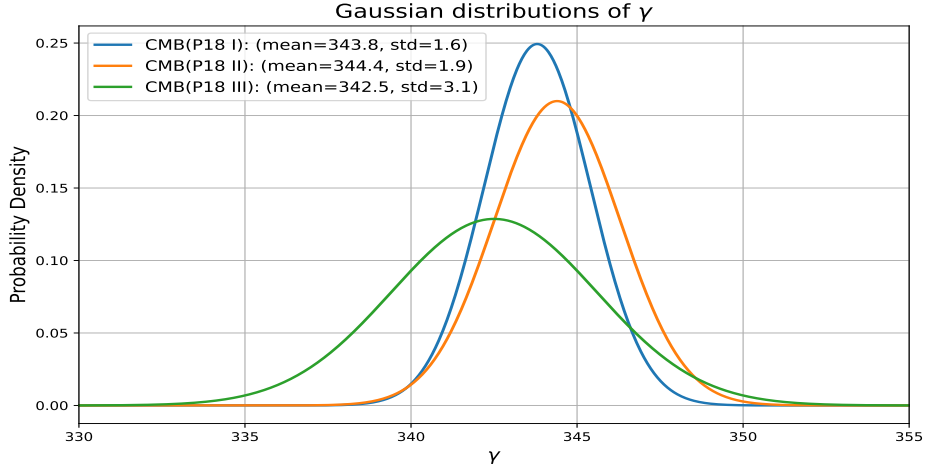


Figure 11. Probability distribution of γ obtained from three CMB distance priors.

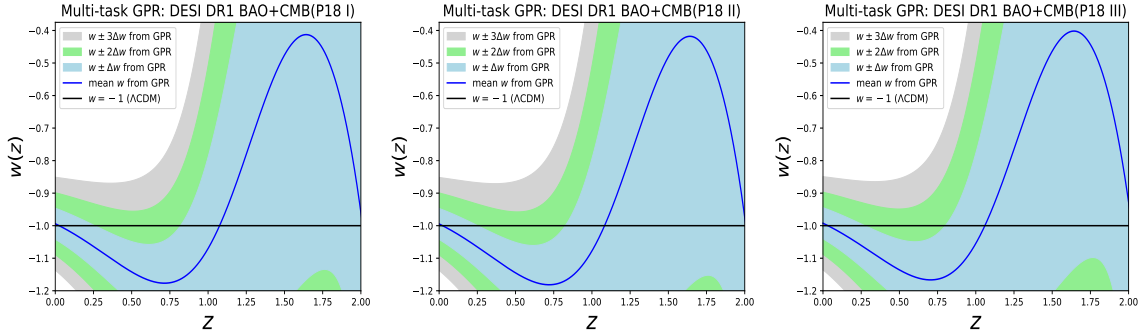


Figure 12. Dark energy equation of state for DESI DR1 BAO combined with three different CMB distance priors.

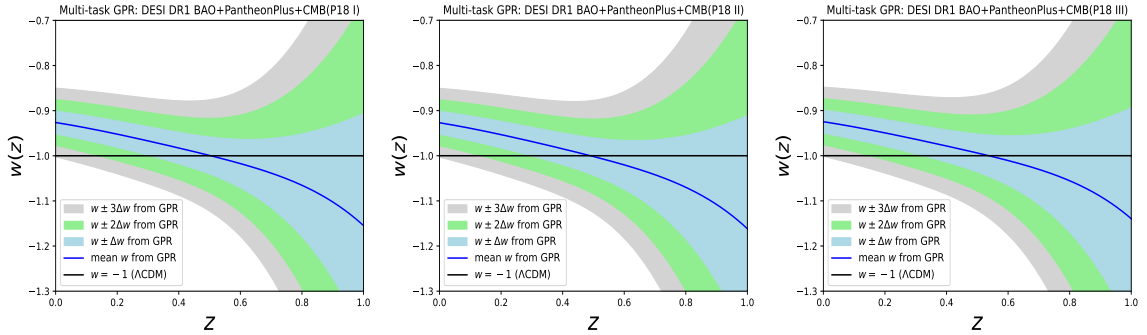


Figure 13. Dark energy equation of state for DESI DR1 BAO+PantheonPlus combined with three different CMB distance priors.

The reason that the results are similar for three different CMB distance priors is that the main contribution to the error in w is from the error in the late-time data, not from the error of early-time data – the error in w from late-time data dominates over that from early-time data. This can be seen if we plot the two contributions separately, by rewriting

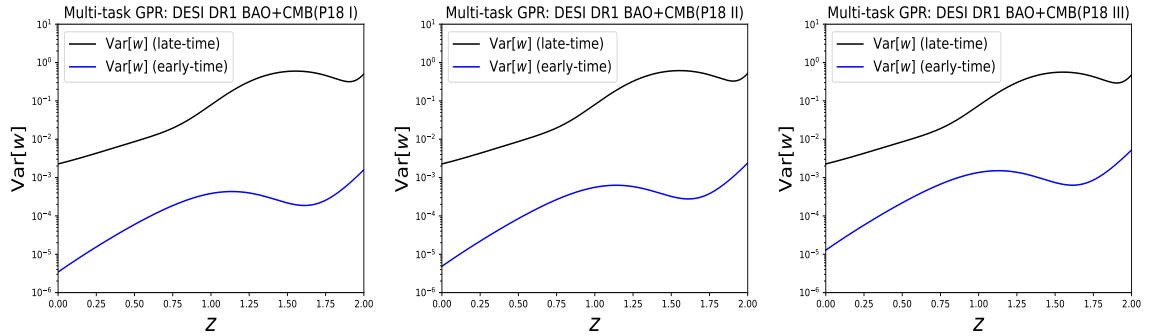


Figure 14. Contribution of error in w (through variance) from error in late-time data (black lines), compared to the error from early-time data (blue lines), for the three CMB distance priors.

the total variance of w as a sum:

$$\text{Var}[w] = \text{Var}[w](\text{late}) + \text{Var}[w](\text{early}), \quad (\text{E.4})$$

$$\text{Var}[w](\text{late}) = \left(\frac{\partial w}{\partial \tilde{D}_H} \right)^2 \text{Var}[\tilde{D}_H] + \left(\frac{\partial w}{\partial \tilde{D}'_H} \right)^2 \text{Var}[\tilde{D}'_H] + 2 \frac{\partial w}{\partial \tilde{D}_H} \frac{\partial w}{\partial \tilde{D}'_H} \text{Cov}[\tilde{D}_H, \tilde{D}'_H], \quad (\text{E.5})$$

$$\text{Var}[w](\text{early}) = \left(\frac{\partial w}{\partial \gamma} \right)^2 \text{Var}[\gamma]. \quad (\text{E.6})$$

Figure 14 displays the late-time (black lines) and early-time (blue lines) variances for three different CMB distance priors. This shows that $\text{Var}[w](\text{late})$ is ~ 3 orders of magnitude larger than $\text{Var}[w](\text{early})$. The standard deviation in the reconstructed w is clearly dominated by errors in the late-time data. Hence the estimation of the standard deviation of w hardly depends on the error in the early CMB data.

The discussions in this section have been done with certain combinations of data, but the conclusion and results are similar for other combinations of data considered in this study.

F Mean function dependence of GPR predictions

Here we explicitly show how the results depend on the different mean functions other than on the zero mean function [83]. We consider three of the main cosmological models: Λ CDM, w CDM, and w_0w_a CDM.

When we reconstruct the errors, we use the full marginalization over all the parameters, i.e., *all parameters of the mean function and all hyper-parameters of the kernel covariance function*. In particular, this is important when the chosen mean function is close to the actual mean values of the data because only using best-fit values of these parameters from the optimization of the log marginal likelihood would have very small error bars in the estimation of any function using GP.

Figure 15 displays the mean and 1σ confidence intervals (standard deviations) of \tilde{D}_M (top row), \tilde{D}_H (middle row), and \tilde{D}'_H (bottom row), for the three mean functions, i.e, zero (left column), Λ CDM (middle column), and w CDM (right column). These are obtained using multi-task GPR on DESI DR1 BAO data. We find no significant differences in these reconstructed functions for three different mean functions, except for \tilde{D}'_H . The predictions of

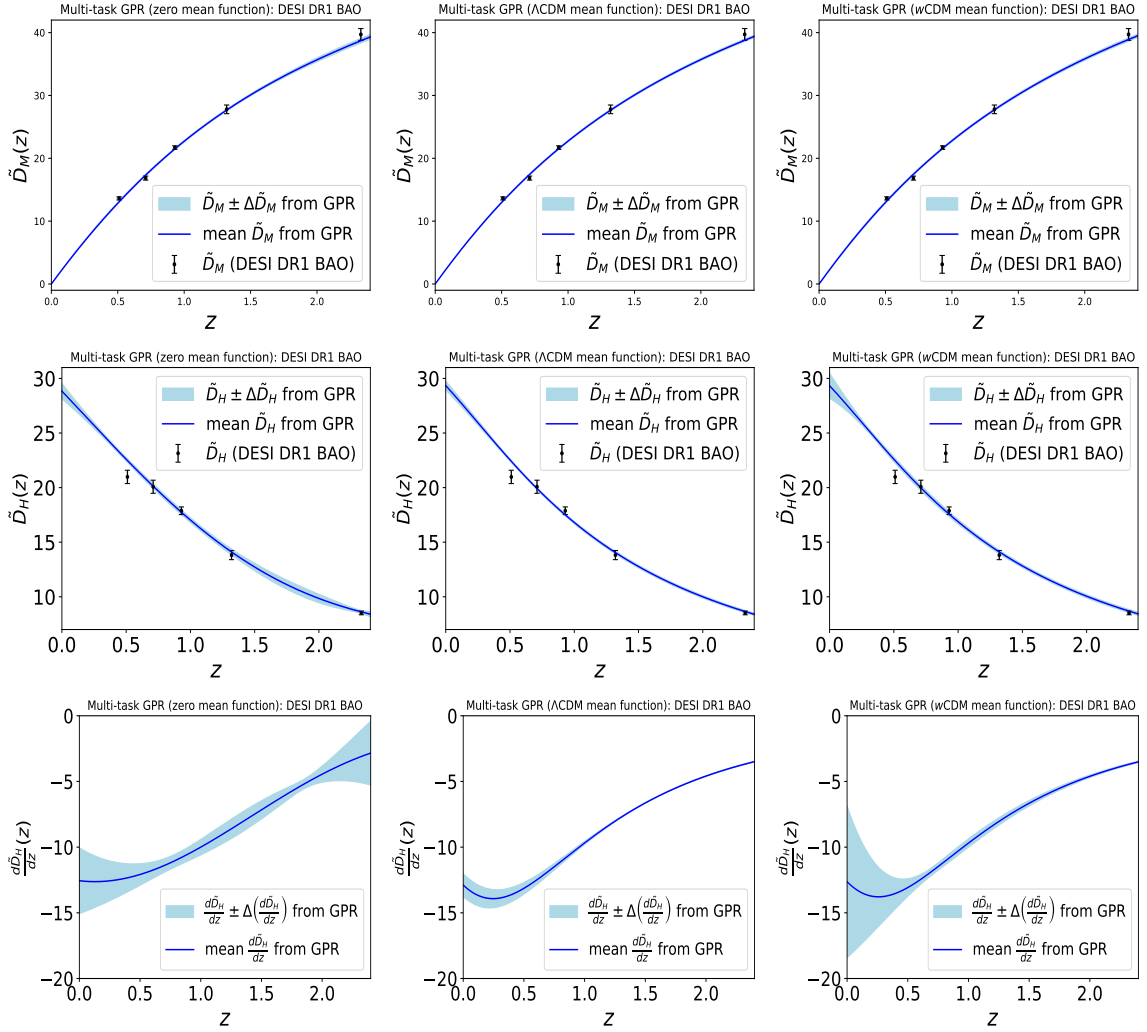


Figure 15. Predictions of multi-task GPR for \tilde{D}_M (top row), \tilde{D}_H (middle row), and \tilde{D}'_H (bottom row), for three mean functions: zero (left column), Λ CDM (middle column), and w CDM (right column), using DESI DR1 BAO data.

\tilde{D}'_H slightly differ we show below that this has minimal impact on the reconstruction of the main quantity of interest, i.e., the dark energy equation of state.

In Fig. 16, we repeat the plots in Fig. 15, but using the combinations of DESI DR1 BAO and PantheonPlus data, and with a fourth mean function, w_0w_a CDM.² We find a similar conclusion as for Fig. 15.

From the reconstructed \tilde{D}_H and \tilde{D}'_H , we compute the (effective) equation of state of dark energy w (as we did before in the main text) with the addition of CMB data for each of the mean functions. For the DESI DR1 BAO and CMB combined data, we plot w and the corresponding 1σ , 2σ , and 3σ confidence regions in Fig. 17. The color combinations are the same as in the main text. We find that the reconstructed mean values of w are slightly different for the different mean functions, but the differences are significantly smaller than the

²We did not include w_0w_a CDM in Fig. 15, since we do not find any proper constraints due to the poor constraining power of DESI DR1 BAO data alone on a general model like w_0w_a CDM.

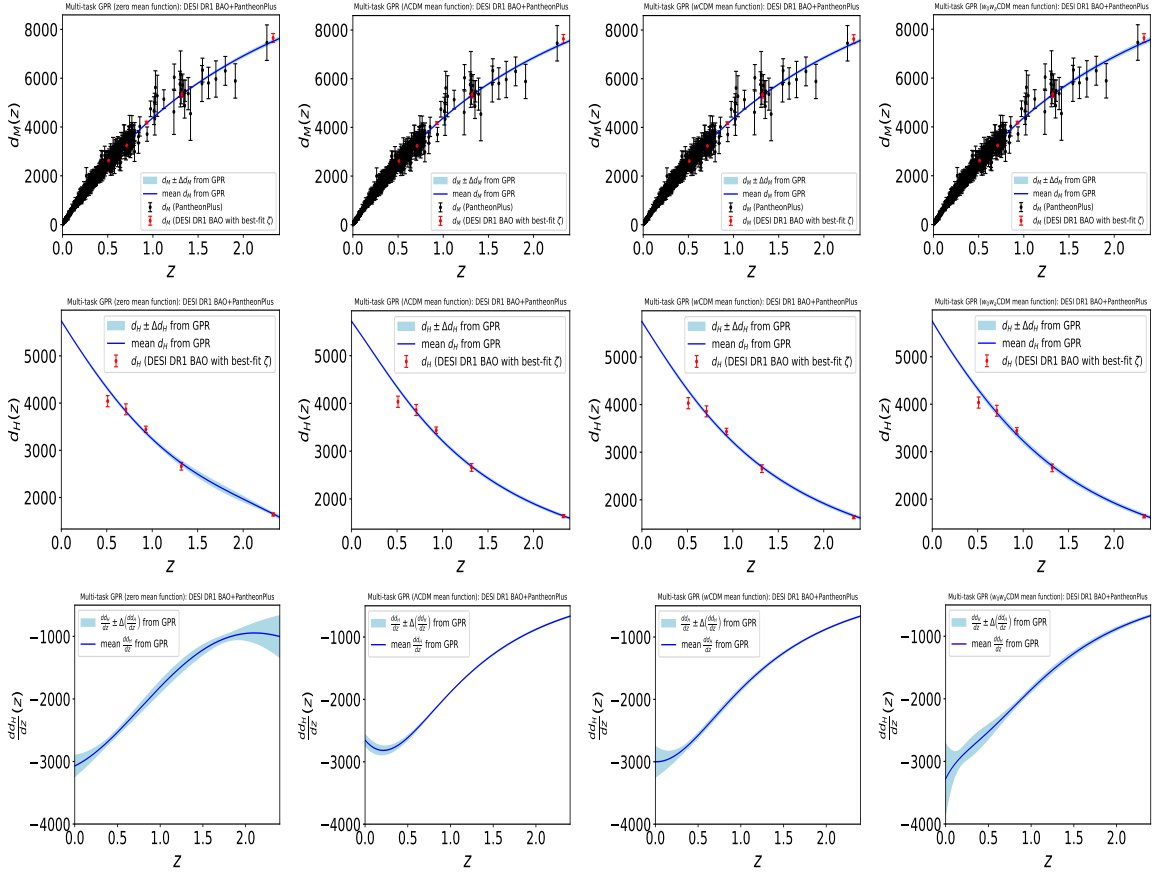


Figure 16. Predictions of multi-task GPR for \tilde{D}_M (top row), \tilde{D}_H (middle row), and \tilde{D}'_H (bottom row) for four mean functions: zero (column 1), Λ CDM (column 2), w CDM (column 3), and w_0w_a CDM (column 4) using DESI DR1 BAO+PantheonPlus data.

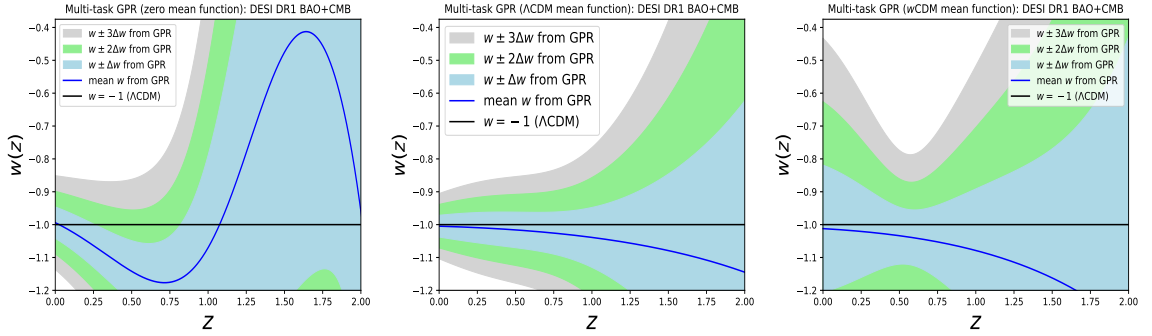


Figure 17. Reconstructed w with the corresponding 1σ , 2σ , and 3σ confidence regions obtained from DESI DR1 BAO+CMB data for three mean functions, as in Fig. 15.

estimated standard deviation corresponding to any of the mean functions. Thus in the sense of statistical confidence, the results are almost similar. This can be stated in another way: that we find no significant evidence of deviation from the Λ CDM model and this conclusion is the same for all three chosen mean functions.

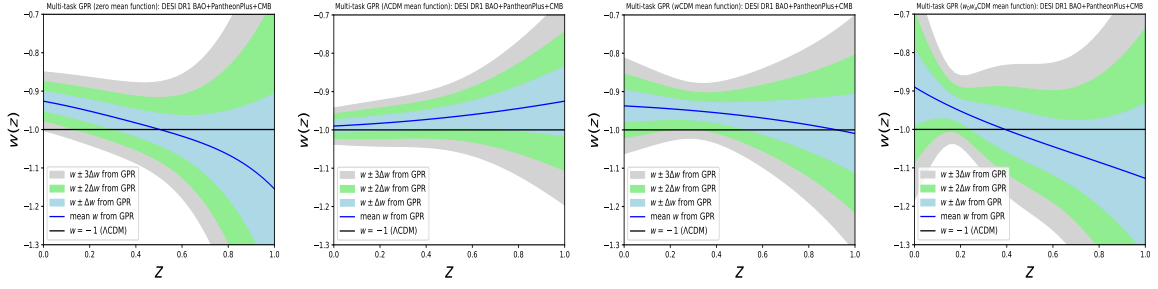


Figure 18. Reconstructed w from DESI DR1 BAO+PantheonPlus+CMB data, with 1, 2, 3 σ confidence regions, for four mean functions, as in Fig. 16.

Figure 18 repeats the plots in Fig. 17, but now with the addition of the PantheonPlus data. We also include the w_0w_a CDM mean function. Similar conclusions apply here: in almost the entire redshift region the Λ CDM model is either $\sim 1\sigma$ away or well within it. This result is significantly independent of the chosen mean function.

Our final comment is that there is no significant evidence of dynamical dark energy and this remains independent of any mean function.

References

- [1] DESI Collaboration, A. G. Adame et al., *DESI 2024 VI: Cosmological Constraints from the Measurements of Baryon Acoustic Oscillations*, [arXiv:2404.03002](#).
- [2] Y. Tada and T. Terada, *Quintessential interpretation of the evolving dark energy in light of DESI observations*, *Phys. Rev. D* **109** (2024), no. 12 L121305, [[arXiv:2404.05722](#)].
- [3] W. Yin, *Cosmic clues: DESI, dark energy, and the cosmological constant problem*, *JHEP* **05** (2024) 327, [[arXiv:2404.06444](#)].
- [4] K. V. Berghaus, J. A. Kable, and V. Miranda, *Quantifying scalar field dynamics with DESI 2024 Y1 BAO measurements*, *Phys. Rev. D* **110** (2024), no. 10 103524, [[arXiv:2404.14341](#)].
- [5] D. Shlivko and P. J. Steinhardt, *Assessing observational constraints on dark energy*, *Phys. Lett. B* **855** (2024) 138826, [[arXiv:2405.03933](#)].
- [6] O. F. Ramadan, J. Sakstein, and D. Rubin, *DESI constraints on exponential quintessence*, *Phys. Rev. D* **110** (2024), no. 4 L041303, [[arXiv:2405.18747](#)].
- [7] I. D. Gialamas, G. Hütsi, K. Kannike, A. Racioppi, M. Raidal, M. Vasar, and H. Veermäe, *Interpreting DESI 2024 BAO: late-time dynamical dark energy or a local effect?*, [arXiv:2406.07533](#).
- [8] V. Patel, A. Chakraborty, and L. Amendola, *The prior dependence of the DESI results*, [arXiv:2407.06586](#).
- [9] D. Wang, *Constraining Cosmological Physics with DESI BAO Observations*, [arXiv:2404.06796](#).
- [10] Y. Yang, X. Ren, Q. Wang, Z. Lu, D. Zhang, Y.-F. Cai, and E. N. Saridakis, *Quintom cosmology and modified gravity after DESI 2024*, *Sci. Bull.* **69** (2024) 2698–2704, [[arXiv:2404.19437](#)].
- [11] C. Escamilla-Rivera and R. Sandoval-Orozco, *$f(T)$ gravity after DESI Baryon acoustic oscillation and DES supernovae 2024 data*, *JHEAp* **42** (2024) 217–221, [[arXiv:2405.00608](#)].
- [12] A. Chudaykin and M. Kunz, *Modified gravity interpretation of the evolving dark energy in light of DESI data*, [arXiv:2407.02558](#).
- [13] O. Luongo and M. Muccino, *Model-independent cosmographic constraints from DESI 2024*, *Astron. Astrophys.* **690** (2024) A40, [[arXiv:2404.07070](#)].
- [14] M. Cortês and A. R. Liddle, *Interpreting DESI’s evidence for evolving dark energy*, *JCAP* **12** (2024) 007, [[arXiv:2404.08056](#)].
- [15] E. O. Colgáin, M. G. Dainotti, S. Capozziello, S. Pourojaghi, M. M. Sheikh-Jabbari, and D. Stojkovic, *Does DESI 2024 Confirm Λ CDM?*, [arXiv:2404.08633](#).
- [16] Y. Carloni, O. Luongo, and M. Muccino, *Does dark energy really revive using DESI 2024 data?*, [arXiv:2404.12068](#).
- [17] D. Wang, *The Self-Consistency of DESI Analysis and Comment on “Does DESI 2024 Confirm Λ CDM?”*, [arXiv:2404.13833](#).
- [18] W. Giarè, M. A. Sabogal, R. C. Nunes, and E. Di Valentino, *Interacting Dark Energy after DESI Baryon Acoustic Oscillation measurements*, [arXiv:2404.15232](#).
- [19] O. Seto and Y. Toda, *DESI constraints on the varying electron mass model and axionlike early dark energy*, *Phys. Rev. D* **110** (2024), no. 8 083501, [[arXiv:2405.11869](#)].
- [20] T.-N. Li, P.-J. Wu, G.-H. Du, S.-J. Jin, H.-L. Li, J.-F. Zhang, and X. Zhang, *Constraints on Interacting Dark Energy Models from the DESI Baryon Acoustic Oscillation and DES Supernovae Data*, *Astrophys. J.* **976** (2024), no. 1 1, [[arXiv:2407.14934](#)].

- [21] F. J. Qu, K. M. Surrao, B. Bolliet, J. C. Hill, B. D. Sherwin, and H. T. Jense, *Accelerated inference on accelerated cosmic expansion: New constraints on axion-like early dark energy with DESI BAO and ACT DR6 CMB lensing*, [arXiv:2404.16805](#).
- [22] H. Wang and Y.-S. Piao, *Dark energy in light of recent DESI BAO and Hubble tension*, [arXiv:2404.18579](#).
- [23] C.-G. Park, J. de Cruz Perez, and B. Ratra, *Using non-DESI data to confirm and strengthen the DESI 2024 spatially-flat w_0w_a CDM cosmological parameterization result*, [arXiv:2405.00502](#).
- [24] **DESI** Collaboration, R. Calderon et al., *DESI 2024: reconstructing dark energy using crossing statistics with DESI DR1 BAO data*, *JCAP* **10** (2024) 048, [[arXiv:2405.04216](#)].
- [25] B. R. Dinda, *A new diagnostic for the null test of dynamical dark energy in light of DESI 2024 and other BAO data*, *JCAP* **09** (2024) 062, [[arXiv:2405.06618](#)].
- [26] **DESI** Collaboration, K. Lodha et al., *DESI 2024: Constraints on Physics-Focused Aspects of Dark Energy using DESI DR1 BAO Data*, [arXiv:2405.13588](#).
- [27] P. Mukherjee and A. A. Sen, *Model-independent cosmological inference post DESI DR1 BAO measurements*, *Phys. Rev. D* **110** (2024), no. 12 123502, [[arXiv:2405.19178](#)].
- [28] L. Pogosian, G.-B. Zhao, and K. Jedamzik, *A Consistency Test of the Cosmological Model at the Epoch of Recombination Using DESI Baryonic Acoustic Oscillation and Planck Measurements*, *Astrophys. J. Lett.* **973** (2024), no. 1 L13, [[arXiv:2405.20306](#)].
- [29] N. Roy, *Dynamical dark energy in the light of DESI 2024 data*, [arXiv:2406.00634](#).
- [30] X. D. Jia, J. P. Hu, and F. Y. Wang, *Uncorrelated estimations of H_0 redshift evolution from DESI baryon acoustic oscillation observations*, [arXiv:2406.02019](#).
- [31] J. J. Heckman, O. F. Ramadan, and J. Sakstein, *First Constraints on a Pixelated Universe in Light of DESI*, [arXiv:2406.04408](#).
- [32] A. Notari, M. Redi, and A. Tesi, *Consistent theories for the DESI dark energy fit*, *JCAP* **11** (2024) 025, [[arXiv:2406.08459](#)].
- [33] G. P. Lynch, L. Knox, and J. Chluba, *DESI observations and the Hubble tension in light of modified recombination*, *Phys. Rev. D* **110** (2024), no. 8 083538, [[arXiv:2406.10202](#)].
- [34] G. Liu, Y. Wang, and W. Zhao, *Impact of LRG1 and LRG2 in DESI 2024 BAO data on dark energy evolution*, [arXiv:2407.04385](#).
- [35] L. Orchard and V. H. Cárdenas, *Probing dark energy evolution post-DESI 2024*, *Phys. Dark Univ.* **46** (2024) 101678, [[arXiv:2407.05579](#)].
- [36] A. Hernández-Almada, M. L. Mendoza-Martínez, M. A. García-Aspeitia, and V. Motta, *Phenomenological emergent dark energy in the light of DESI Data Release 1*, *Phys. Dark Univ.* **46** (2024) 101668, [[arXiv:2407.09430](#)].
- [37] S. Pourojaghi, M. Malekjani, and Z. Davari, *Cosmological constraints on dark energy parametrizations after DESI 2024: Persistent deviation from standard Λ CDM cosmology*, [arXiv:2407.09767](#).
- [38] U. Mukhopadhyay, S. Haridasu, A. A. Sen, and S. Dhawan, *Inferring dark energy properties from the scale factor parametrisation*, [arXiv:2407.10845](#).
- [39] G. Ye, M. Martinelli, B. Hu, and A. Silvestri, *Non-minimally coupled gravity as a physically viable fit to DESI 2024 BAO*, [arXiv:2407.15832](#).
- [40] W. Giarè, M. Najafi, S. Pan, E. Di Valentino, and J. T. Firouzjaee, *Robust preference for Dynamical Dark Energy in DESI BAO and SN measurements*, *JCAP* **10** (2024) 035, [[arXiv:2407.16689](#)].

- [41] M. Chevallier and D. Polarski, *Accelerating universes with scaling dark matter*, *Int. J. Mod. Phys. D* **10** (2001) 213–224, [[gr-qc/0009008](#)].
- [42] E. V. Linder, *Exploring the expansion history of the universe*, *Phys. Rev. Lett.* **90** (2003) 091301, [[astro-ph/0208512](#)].
- [43] W. J. Wolf and P. G. Ferreira, *Underdetermination of dark energy*, *Phys. Rev. D* **108** (2023), no. 10 103519, [[arXiv:2310.07482](#)].
- [44] R. R. Caldwell, R. Dave, and P. J. Steinhardt, *Cosmological imprint of an energy component with general equation of state*, *Phys. Rev. Lett.* **80** (1998) 1582–1585, [[astro-ph/9708069](#)].
- [45] I. Zlatev, L.-M. Wang, and P. J. Steinhardt, *Quintessence, cosmic coincidence, and the cosmological constant*, *Phys. Rev. Lett.* **82** (1999) 896–899, [[astro-ph/9807002](#)].
- [46] S. Tsujikawa, *Quintessence: A Review*, *Class. Quant. Grav.* **30** (2013) 214003, [[arXiv:1304.1961](#)].
- [47] B. R. Dinda and A. A. Sen, *Imprint of thawing scalar fields on the large scale galaxy overdensity*, *Phys. Rev. D* **97** (2018), no. 8 083506, [[arXiv:1607.05123](#)].
- [48] C. García-García, E. Bellini, P. G. Ferreira, D. Traykova, and M. Zumalacárregui, *Theoretical priors in scalar-tensor cosmologies: Thawing quintessence*, *Phys. Rev. D* **101** (2020), no. 6 063508, [[arXiv:1911.02868](#)].
- [49] G. Ellis, R. Maartens, and M. A. H. MacCallum, *Causality and the speed of sound*, *Gen. Rel. Grav.* **39** (2007) 1651–1660, [[gr-qc/0703121](#)].
- [50] L. Amendola, C. Quercellini, D. Tocchini-Valentini, and A. Pasqui, *Constraints on the interaction and selfinteraction of dark energy from cosmic microwave background*, *Astrophys. J. Lett.* **583** (2003) L53, [[astro-ph/0205097](#)].
- [51] T. Clemson, K. Koyama, G.-B. Zhao, R. Maartens, and J. Valiviita, *Interacting Dark Energy – constraints and degeneracies*, *Phys. Rev. D* **85** (2012) 043007, [[arXiv:1109.6234](#)].
- [52] A. Poursidou, C. Skordis, and E. J. Copeland, *Models of dark matter coupled to dark energy*, *Phys. Rev. D* **88** (2013), no. 8 083505, [[arXiv:1307.0458](#)].
- [53] R. Murgia, S. Gariazzo, and N. Fornengo, *Constraints on the Coupling between Dark Energy and Dark Matter from CMB data*, *JCAP* **04** (2016) 014, [[arXiv:1602.01765](#)].
- [54] E. Di Valentino, A. Melchiorri, O. Mena, and S. Vagnozzi, *Interacting dark energy in the early 2020s: A promising solution to the H_0 and cosmic shear tensions*, *Phys. Dark Univ.* **30** (2020) 100666, [[arXiv:1908.04281](#)].
- [55] S. Tsujikawa, *Modified gravity models of dark energy*, *Lect. Notes Phys.* **800** (2010) 99–145, [[arXiv:1101.0191](#)].
- [56] T. Clifton, P. G. Ferreira, A. Padilla, and C. Skordis, *Modified Gravity and Cosmology*, *Phys. Rept.* **513** (2012) 1–189, [[arXiv:1106.2476](#)].
- [57] K. Koyama, *Cosmological Tests of Modified Gravity*, *Rept. Prog. Phys.* **79** (2016), no. 4 046902, [[arXiv:1504.04623](#)].
- [58] L. Perenon, M. Martinelli, R. Maartens, S. Camera, and C. Clarkson, *Measuring dark energy with expansion and growth*, *Phys. Dark Univ.* **37** (2022) 101119, [[arXiv:2206.12375](#)].
- [59] B. R. Dinda and N. Banerjee, *A comprehensive data-driven odyssey to explore the equation of state of dark energy*, *Eur. Phys. J. C* **84** (2024), no. 7 688, [[arXiv:2403.14223](#)].
- [60] C. Williams and C. Rasmussen, *Gaussian processes for regression*, *Advances Neural Information Processing Systems* **8** (1995).
- [61] C. Rasmussen and C. Williams, *Gaussian Processes for Machine Learning*. MIT Press, 2006.

- [62] A. Shafieloo, A. G. Kim, and E. V. Linder, *Gaussian Process Cosmography*, *Phys. Rev. D* **85** (2012) 123530, [[arXiv:1204.2272](#)].
- [63] M. Seikel, C. Clarkson, and M. Smith, *Reconstruction of dark energy and expansion dynamics using Gaussian processes*, *JCAP* **06** (2012) 036, [[arXiv:1204.2832](#)].
- [64] B. S. Haridasu, V. V. Luković, M. Moresco, and N. Vittorio, *An improved model-independent assessment of the late-time cosmic expansion*, *JCAP* **10** (2018) 015, [[arXiv:1805.03595](#)].
- [65] P. Mukherjee and N. Banerjee, *Non-parametric reconstruction of the cosmological jerk parameter*, *Eur. Phys. J. C* **81** (2021), no. 1 36, [[arXiv:2007.10124](#)].
- [66] eBOSS Collaboration, R. E. Keeley, A. Shafieloo, G.-B. Zhao, J. A. Vazquez, and H. Koo, *Reconstructing the Universe: Testing the Mutual Consistency of the Pantheon and SDSS/eBOSS BAO Data Sets with Gaussian Processes*, *Astron. J.* **161** (2021), no. 3 151, [[arXiv:2010.03234](#)].
- [67] L. Perenon, M. Martinelli, S. Ilić, R. Maartens, M. Lochner, and C. Clarkson, *Multi-tasking the growth of cosmological structures*, *Phys. Dark Univ.* **34** (2021) 100898, [[arXiv:2105.01613](#)].
- [68] B. R. Dinda, *Minimal model-dependent constraints on cosmological nuisance parameters and cosmic curvature from combinations of cosmological data*, *Int. J. Mod. Phys. D* **32** (2023), no. 11 2350079, [[arXiv:2209.14639](#)].
- [69] M. A. Sabogal, O. Akarsu, A. Bonilla, E. Di Valentino, and R. C. Nunes, *Exploring new physics in the late Universe’s expansion through non-parametric inference*, *Eur. Phys. J. C* **84** (2024), no. 7 703, [[arXiv:2407.04223](#)].
- [70] DESI Collaboration, R. Zhou et al., *Target Selection and Validation of DESI Luminous Red Galaxies*, *Astron. J.* **165** (2023), no. 2 58, [[arXiv:2208.08515](#)].
- [71] A. Raichoor et al., *Target Selection and Validation of DESI Emission Line Galaxies*, *Astron. J.* **165** (2023), no. 3 126, [[arXiv:2208.08513](#)].
- [72] BOSS Collaboration, S. Alam et al., *The clustering of galaxies in the completed SDSS-III Baryon Oscillation Spectroscopic Survey: cosmological analysis of the DR12 galaxy sample*, *Mon. Not. Roy. Astron. Soc.* **470** (2017), no. 3 2617–2652, [[arXiv:1607.03155](#)].
- [73] eBOSS Collaboration, S. Alam et al., *Completed SDSS-IV extended Baryon Oscillation Spectroscopic Survey: Cosmological implications from two decades of spectroscopic surveys at the Apache Point Observatory*, *Phys. Rev. D* **103** (2021), no. 8 083533, [[arXiv:2007.08991](#)].
- [74] eBOSS Collaboration, J. Hou et al., *The Completed SDSS-IV extended Baryon Oscillation Spectroscopic Survey: BAO and RSD measurements from anisotropic clustering analysis of the Quasar Sample in configuration space between redshift 0.8 and 2.2*, *Mon. Not. Roy. Astron. Soc.* **500** (2020), no. 1 1201–1221, [[arXiv:2007.08998](#)].
- [75] eBOSS Collaboration, H. du Mas des Bourboux et al., *The Completed SDSS-IV Extended Baryon Oscillation Spectroscopic Survey: Baryon Acoustic Oscillations with Ly α Forests*, *Astrophys. J.* **901** (2020), no. 2 153, [[arXiv:2007.08995](#)].
- [76] W. Hu and N. Sugiyama, *Small scale cosmological perturbations: An Analytic approach*, *Astrophys. J.* **471** (1996) 542–570, [[astro-ph/9510117](#)].
- [77] L. Chen, Q.-G. Huang, and K. Wang, *Distance Priors from Planck Final Release*, *JCAP* **02** (2019) 028, [[arXiv:1808.05724](#)].
- [78] Z. Zhai, C.-G. Park, Y. Wang, and B. Ratra, *CMB distance priors revisited: effects of dark energy dynamics, spatial curvature, primordial power spectrum, and neutrino parameters*, *JCAP* **07** (2020) 009, [[arXiv:1912.04921](#)].

- [79] Z. Zhai and Y. Wang, *Robust and model-independent cosmological constraints from distance measurements*, *JCAP* **07** (2019) 005, [[arXiv:1811.07425](#)].
- [80] **Planck** Collaboration, N. Aghanim et al., *Planck 2018 results. VI. Cosmological parameters*, *Astron. Astrophys.* **641** (2020) A6, [[arXiv:1807.06209](#)]. [Erratum: *Astron. Astrophys.* 652, C4 (2021)].
- [81] D. Scolnic et al., *The Pantheon+ Analysis: The Full Data Set and Light-curve Release*, *Astrophys. J.* **938** (2022), no. 2 113, [[arXiv:2112.03863](#)].
- [82] D. Brout et al., *The Pantheon+ Analysis: Cosmological Constraints*, *Astrophys. J.* **938** (2022), no. 2 110, [[arXiv:2202.04077](#)].
- [83] S.-g. Hwang, B. L’Huillier, R. E. Keeley, M. J. Jee, and A. Shafieloo, *How to use GP: effects of the mean function and hyperparameter selection on Gaussian process regression*, *JCAP* **02** (2023) 014, [[arXiv:2206.15081](#)].
- [84] A. Heinesen, C. Blake, and D. L. Wiltshire, *Quantifying the accuracy of the Alcock-Paczynski scaling of baryon acoustic oscillation measurements*, *JCAP* **01** (2020) 038, [[arXiv:1908.11508](#)].
- [85] J. L. Bernal, T. L. Smith, K. K. Boddy, and M. Kamionkowski, *Robustness of baryon acoustic oscillation constraints for early-Universe modifications of Λ CDM cosmology*, *Phys. Rev. D* **102** (2020), no. 12 123515, [[arXiv:2004.07263](#)].
- [86] J. Pan, D. Huterer, F. Andrade-Oliveira, and C. Avestruz, *Compressed baryon acoustic oscillation analysis is robust to modified-gravity models*, *JCAP* **06** (2024) 051, [[arXiv:2312.05177](#)].
- [87] S. Anselmi, G. D. Starkman, and A. Renzi, *Cosmological forecasts for future galaxy surveys with the linear point standard ruler: Toward consistent bAO analyses far from a fiducial cosmology*, *Phys. Rev. D* **107** (Jun, 2023) 123506.
- [88] M. O’Dwyer, S. Anselmi, G. D. Starkman, P.-S. Corasaniti, R. K. Sheth, and I. Zehavi, *Linear point and sound horizon as purely geometric standard rulers*, *Phys. Rev. D* **101** (Apr, 2020) 083517.
- [89] E. Di Valentino, O. Mena, S. Pan, L. Visinelli, W. Yang, A. Melchiorri, D. F. Mota, A. G. Riess, and J. Silk, *In the realm of the Hubble tension—a review of solutions*, *Class. Quant. Grav.* **38** (2021), no. 15 153001, [[arXiv:2103.01183](#)].
- [90] S. Vagnozzi, *New physics in light of the H_0 tension: An alternative view*, *Phys. Rev. D* **102** (2020), no. 2 023518, [[arXiv:1907.07569](#)].
- [91] C. Krishnan, R. Mohayaee, E. O. Colgáin, M. M. Sheikh-Jabbari, and L. Yin, *Does Hubble tension signal a breakdown in FLRW cosmology?*, *Class. Quant. Grav.* **38** (2021), no. 18 184001, [[arXiv:2105.09790](#)].
- [92] D. Camarena and V. Marra, *On the use of the local prior on the absolute magnitude of Type Ia supernovae in cosmological inference*, *Mon. Not. Roy. Astron. Soc.* **504** (2021) 5164–5171, [[arXiv:2101.08641](#)].
- [93] G. Efstathiou, *To H_0 or not to H_0 ?*, *Mon. Not. Roy. Astron. Soc.* **505** (2021), no. 3 3866–3872, [[arXiv:2103.08723](#)].
- [94] B. R. Dinda, *Cosmic expansion parametrization: Implication for curvature and H_0 tension*, *Phys. Rev. D* **105** (2022), no. 6 063524, [[arXiv:2106.02963](#)].
- [95] Z. Sakr, *Testing the hypothesis of a matter density discrepancy within Λ CDM model using multiple probes*, *Phys. Rev. D* **108** (2023), no. 8 083519, [[arXiv:2305.02846](#)].
- [96] B. R. Dinda, *Analytical Gaussian process cosmography: unveiling insights into matter-energy density parameter at present*, *Eur. Phys. J. C* **84** (2024), no. 4 402, [[arXiv:2311.13498](#)].

- [97] Y. Chen, S. Kumar, B. Ratra, and T. Xu, *Effects of Type Ia Supernovae Absolute Magnitude Priors on the Hubble Constant Value*, *Astrophys. J. Lett.* **964** (2024), no. 1 L4, [[arXiv:2401.13187](#)].
- [98] A. G. Riess et al., *A Comprehensive Measurement of the Local Value of the Hubble Constant with 1 km/s/Mpc Uncertainty from the Hubble Space Telescope and the SH0ES Team*, *Astrophys. J. Lett.* **934** (2022), no. 1 L7, [[arXiv:2112.04510](#)].
- [99] B. R. Dinda and N. Banerjee, *Model independent bounds on type Ia supernova absolute peak magnitude*, *Phys. Rev. D* **107** (2023), no. 6 063513, [[arXiv:2208.14740](#)].
- [100] Y. Wang, *Flux-averaging analysis of type ia supernova data*, *Astrophys. J.* **536** (2000) 531, [[astro-ph/9907405](#)].
- [101] **Supernova Search Team** Collaboration, A. G. Riess et al., *Observational evidence from supernovae for an accelerating universe and a cosmological constant*, *Astron. J.* **116** (1998) 1009–1038, [[astro-ph/9805201](#)].
- [102] V. Poulin, T. L. Smith, R. Calderón, and T. Simon, *On the implications of the ‘cosmic calibration tension’ beyond H_0 and the synergy between early- and late-time new physics*, [[arXiv:2407.18292](#)].
- [103] D. Pedrotti, J.-Q. Jiang, L. A. Escamilla, S. S. da Costa, and S. Vagnozzi, *Multidimensionality of the Hubble tension: the roles of Ω_m and ω_c* , [[arXiv:2408.04530](#)].